remote sensing

MDPI

Article

Tracking the Seismic Deformation of Himalayan Glaciers Using Synthetic Aperture Radar Interferometry

Sandeep Kumar Mondal [1,2], Rishikesh Bharti [1,2] and Kristy F. Tiampo [3,*]

[1] Technology Innovation Hub (TIH), Technology Innovation and Development Foundation (TIDF), Indian Institute of Technology, Guwahati 781039, Assam, India; sandeepkumar@alumni.iitg.ac.in (S.K.M.); rbharti@iitg.ac.in (R.B.)
[2] Earth System Science and Engineering Division, Department of Civil Engineering, Indian Institute of Technology, Guwahati 781039, Assam, India
[3] Department of Geological Sciences, University of Colorado Boulder, Boulder, CO 80309, USA
* Correspondence: kristy.tiampo@colorado.edu

Abstract: The Himalayan belt, formed due to the Cenozoic convergence between the Eurasian and Indian craton, acts as a storehouse of large amounts of strain, resulting in large earthquakes from the Western to the Eastern Himalayas. Glaciers also occur over a major portion of the high-altitude Himalayan region. The impact of earthquakes can be easily studied in the plains and plateaus with the help of well-distributed seismogram networks and these regions' accessibility is helpful for field- and lab-based studies. However, earthquakes triggered close to high-altitude Himalayan glaciers are tough to investigate for the impact over glaciers and glacial deposits. In this study, we attempt to understand the impact of earthquakes on and around Himalayan glaciers in terms of vertical displacement and coherence change using space-borne synthetic aperture radar (SAR). Eight earthquake events of various magnitudes and hypocenter depths occurring in the vicinity of Himalayan glacial bodies were studied using C-band Sentinel1-A/B SAR data. Differential interferometric SAR (DInSAR) analysis is applied to capture deformation of the glacial surface potentially related to earthquake occurrence. Glacial displacement varies from −38.9 mm to −5.4 mm for the 2020 Tibet earthquake (M_w 5.7) and the 2021 Nepal earthquake (M_w 4.1). However, small glacial and ground patches processed separately for vertical displacements reveal that the glacial mass shows much greater seismic displacement than the ground surface. This indicates the possibility of the presence of potential site-specific seismicity amplification properties within glacial bodies. A reduction in co-seismic coherence around the glaciers is observed in some cases, indicative of possible changes in the glacial moraine deposits and/or vegetation cover. The effect of two different seismic events (the 2020 and 2021 Nepal earthquakes) with different hypocenter depths but with the same magnitude at almost equal distances from the glaciers is assessed; a shallow earthquake is observed to result in a larger impact on glacial bodies in terms of vertical displacement. Earthquakes may induce glacial hazards such as glacial surging, ice avalanches, and the failure of moraine-/ice-dammed glacial lakes. This research may be able to play a possible role in identifying areas at risk and provide valuable insights for the planning and implementation of measures for disaster risk reduction.

Keywords: earthquake; Himalayas; glacier; synthetic aperture radar (SAR); InSAR; coherence

check for updates

Academic Editor: Michele Saroli

Received: 28 December 2024
Revised: 25 February 2025
Accepted: 28 February 2025
Published: 5 March 2025

Citation: Mondal, S.K.; Bharti, R.; Tiampo, K.F. Tracking the Seismic Deformation of Himalayan Glaciers Using Synthetic Aperture Radar Interferometry. *Remote Sens.* **2025**, *17*, 911. https://doi.org/10.3390/rs17050911

Copyright: © 2025 by the authors. Licensee MDPI, Basel, Switzerland. This article is an open access article distributed under the terms and conditions of the Creative Commons Attribution (CC BY) license (https://creativecommons.org/licenses/by/4.0/).

1. Introduction

Glaciers are the perennial storehouse of freshwater in high altitudes/low latitudes. Apart from the polar cryosphere, the Himalayan cryosphere has the largest glacial coverage, accounting for an area of ~33,000 km^2 [1]. Glaciers behave differently in different seasons, and glacier dynamics (flow velocities) vary seasonally due to enhanced melting rates in the ablation period and reduced melting in the accumulation period [2–5]. Glacial dynamics also include surface mobility, glacial facies, and changes in the areal extent and elevation profile, and spaceborne/airborne remote sensing techniques have been studied extensively [6–11]. Glaciological investigations conducted using field-based and satellite-driven studies have shown that the Himalayan glaciers behave in synchronization with various meteorological parameters such as temperature and precipitation, resulting in retreat and negative mass balance [12–16]. These glaciers are located in the Eastern and Western Himalayas' challenging, inaccessible, and seismically prone areas.

Earthquake impact assessment is a crucial task conducted after seismic events. The most common approach for determining earthquake magnitude and aftereffects is the analysis of ground-based seismometer datasets. However, due to their limited deployment in high-altitude glaciated regions, it is difficult to study certain earthquake events that occur close to those glacial bodies. Therefore, several geophysicists and seismologists have supplemented ground-based methods with geodetic and satellite remote sensing-based approaches [17].

The routine assessment of damage and continuous monitoring through the synoptic acquisition of data and analysis is essential in the study of natural hazards, particularly earthquakes in the remote glaciated regions of Himalayan ranges which are sudden, unpredictable, and are capable of activating other hazards such as avalanches, glacial lake outburst floods, and landslides. Therefore, extensive monitoring at high temporal and spatial resolution is essential, using techniques such as differential global positioning systems (DGPSs), photogrammetry, and optical remote sensing. Radar technology, due to its cloud penetrating capacity, is advantageous for all-weather glaciological monitoring and proves to be more suited for studying the rugged and valley-adorned terrain of mountainous regions such as the Himalayas [18,19]. Radar interferometry has been an effective technique in the study of the Himalayan cryosphere and in the study of associated natural hazards such as avalanches [20,21], slope failures [22], glacial lake outburst floods [23–25], landslides [26–28], and earthquakes [29–31]. The pros and cons of these microwave bands are derived from the sensor wavelength. The shorter the wavelength, the better the spatial resolution, whereas the longer the wavelength, the better the surface penetration [32,33].

There are various techniques in microwave remote sensing to measure glacial surface velocity, such as SAR interferometry [7], multiple aperture interferometry (MAI) [34], and offset tracking [19]. For tracking glacial surface displacement in time, DInSAR is an important technique, provided there exist short temporal and geometrical baselines [31]. DInSAR is a very effective method for analyzing surface deformations due to subsidence, landslides, earthquake-triggered slope failures, glacial velocity, and other natural hazards [35–40]. For the Himalayan glaciers, offset tracking and DInSAR are the most common and widely used techniques [41–44]. In earthquake research, DInSAR has been used to estimate the co-seismic deformation field [45,46]. In recent times, DInSAR has become a preferred technique for deriving the precise surface deformation of glaciers on a temporal basis [47,48].

In this paper, we study the impact of seismic events on and around glacial bodies situated in different parts of the Himalayan region using DInSAR. Various earthquakes of different magnitudes and hypocenter depths that occurred in close proximity to glacial bodies were investigated for seismic deformation. The main contributions are as follows:

- The detection of seismic deformation in glacial bodies using DInSAR.
- The increased deformation in glacial bodies over that of the ground surface was noted, suggesting the potential seismic amplification properties of glaciers.

The remainder of the presented work is organized as follows: Section 2 provides details of the study area. Section 3 outlines the datasets and methods adopted in the study. Sections 4 and 5 present the results and discussion, respectively. Section 6 presents the conclusion.

2. Study Area

The collision between the Indian and Eurasian plates during the Cenozoic period resulted in the formation of two major orogenic features, the Tibetan plateau and the Himalaya–Hindu Kush mountains [49]. The Himalayan orogeny falls into the category of being an active orogenic belt with geological and geomorphic structures of the Quaternary–Holocene age [50]. Three principal thrusts, namely the main central thrust (MCT) [51], the main boundary thrust (MBT) [52], and the Himalayan frontal thrust (HFT) [53], developed progressively in the early Miocene, late Miocene, and Quaternary periods, respectively. The Himalayan arc and its contiguous emergent structures are seismically active and have resulted in very large seismic events in the recent past, including devastating earthquakes such as the 1897 Shillong (M_w 8.1), the 1905 Kangra (M_w 7.8), the 1934 Bihar–Nepal (M_w 8.2), and the 1950 Assam (M_w 8.6) earthquakes. In the present study, we are investigating glacial deformation potentially caused by earthquake activity. Eight earthquake events of different magnitudes, hypocenter depths, and epicenter locations that have occurred in the recent past and are close to the Himalayan glacial bodies are considered here, as shown in Figure 1 and Table 1. We performed DInSAR analysis of two other events, the 2023 Nepal earthquake and the 2024 China earthquake, but in these cases, while solid earth deformation was identified, no deformations of local glaciers were observed in the resulting interferograms [54].

Table 1. Details of earthquake events in this study.

Events	Date/UTC Time	Epicenter Location	Seismic Magnitude (M_w)	Hypocenter Depth (km)
Tibet Earthquake	20 March 2020/01:33:15	28.590°N 87.308°E	5.7	10
Leh Earthquake	25 September 2020/10:57:13	34.249°N 78.206°E	5.3	10
Thang Earthquake	6 December 2017/23:29:03	35.724°N 77.562°E	5.2	74.3
Joshimath Earthquake	23 May 2021/19:01:39	30.876°N 79.271°E	4.5	10
Sikkim Earthquake	17 June 2018/15:07:37	27.420°N 88.474°E	4.4	49.8
Sikkim Earthquake	16 May 2017/22:13:19	27.327°N 88.171°E	4.2	10
Nepal Earthquake	8 November 2020/21:44:14	27.730°N 87.771°E	4.1	10
Nepal Earthquake	11 January 2021/13:59:49	28.028°N 87.789°E	4.1	35

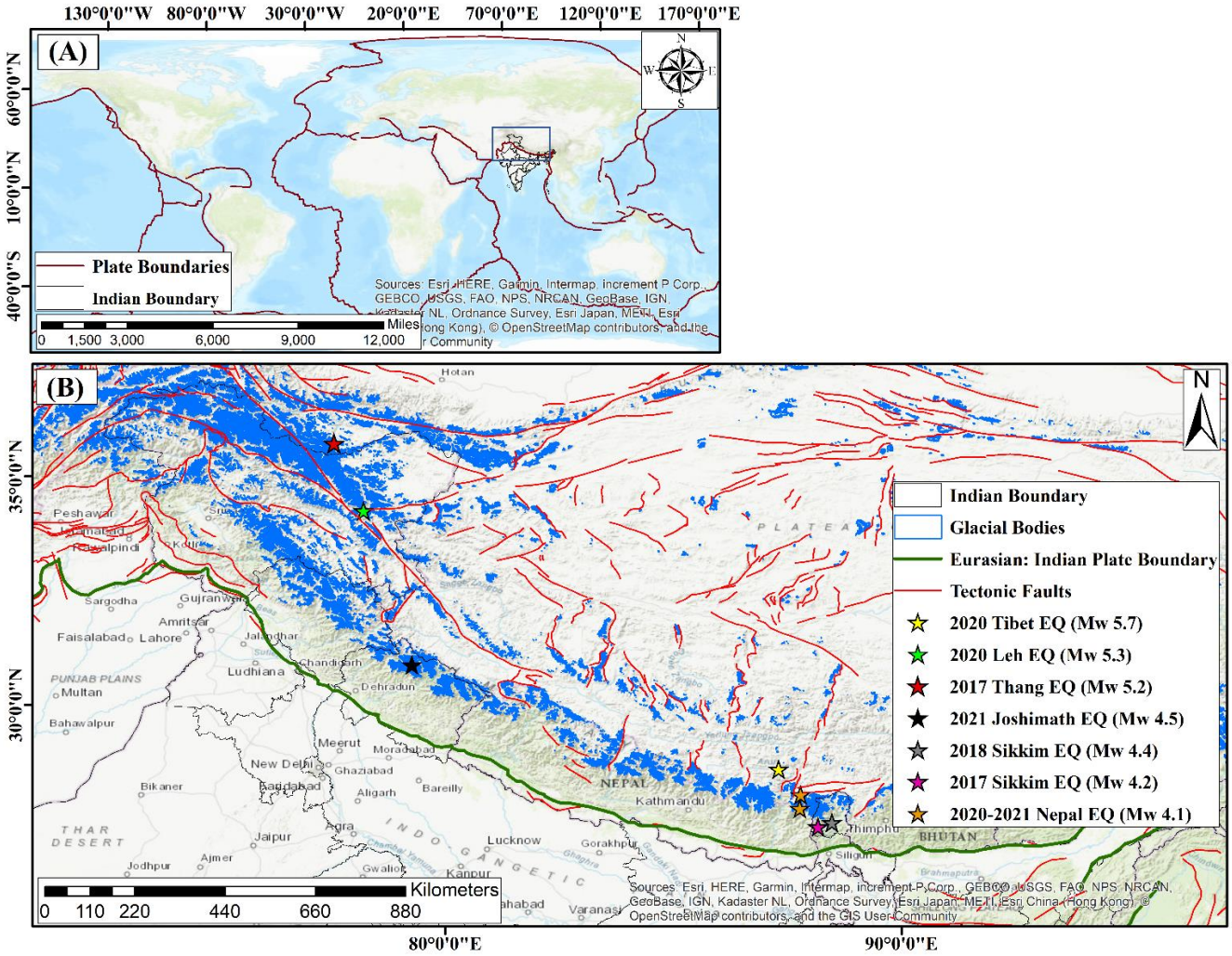


Figure 1. Study area map showing (**A**) world map with geographical boundary of India, tectonic plate boundaries, and (**B**) the Himalayan glaciers, tectonic lineaments, Indian–Eurasian plate boundaries, and selected earthquake epicenters (sources: Esri, HERE, Garmin International, and others as mentioned on the map).

3. Data and Methods

3.1. Data

Sentinel-1A/B SAR datasets were used in this study. Developed by the European Space Agency (ESA), Sentinel-1A/B is a dual satellite configuration that acquires data in the microwave C-band (λ: 5.6 cm, f: 5.405 GHz) [55]. Both satellites lie in the same orbit plane with a combined and individual temporal resolution of 6 and 12 days, respectively. Several data formats are provided by Sentinel-1A/B, including Level-1 Ground Range Detection (GRD), Level-2 Ocean (OCN), and Level-0 and Level-1 Single Look Complex (SLC). It also has various modes of operation, namely Wave (WV), Strip Map (SM), Extra Wide Swath (EW), and Interferometric Wide Swath (IW) modes. The IW mode captures data in a 250 km swath with a spatial resolution of approximately 5 m × 20 m [56]. In this study, we used pre- and co-seismic pairs of SLC datasets, as shown in Table 2. Sentinel-2 Level-1C (L1C) multispectral instrument (MSI) data from the Nepal earthquake region on 17 January 2021 was also used to observe the vegetation coverage through a false-color-composite (FCC) image. Here, green (543–578 nm) and red (658–680 nm) bands at 10 m and the near-infrared (785–899 nm) band at a 20 m resolution have been used to generate a false-color-composite

(FCC) image of the zone of study. The boundary of the Himalayan glacial bodies has been adopted from the Randolph glacial inventory, RGI 6.0 [57].

Table 2. Sentinel-1A/B C-band SLC images used in this study.

Sentinel 1 SLC Datasets							
Year-Earthquake	**Pre-Earthquake Datasets**		**Co-Earthquake Datasets**		**Beam Mode-Subswath/Flight Direction**	**Frame/Path**	**Polarization**
	Primary	**Secondary**	**Primary**	**Secondary**			
2020-Tibet Earthquake	04-03-2020	16-03-2020	16-03-2020	28-03-2020	IW-1/Descending	496/121	VV+VH
2020-Leh Earthquake	07-09-2020	19-09-2020	19-09-2020	01-10-2020	IW-1/Descending	476/136	VV+VH
2017-Thang Earthquake	15-11-2017	27-11-2017	27-11-2017	09-12-2017	IW-1,2/Ascending	112/129	VV+VH
2021-Joshirmath Earthquake	06-05-2021	18-05-2021	18-05-2021	30-05-2021	IW-1,2/Descending	487/63	VV+VH
2018-Sikkim Earthquake	30-05-2018	11-06-2018	11-06-2018	23-06-2018	IW-3/Descending	84/12	VV+VH
2017-Sikkim Earthquake	02-05-2017	14-05-2017	14-05-2017	26-05-2017	IW-2/Descending	499/48	VV+VH
2020-Nepal Earthquake	25-10-2020	06-11-2020	06-11-2020	18-11-2020	IW-3/Descending	499/48	VV+VH
2021-Nepal Earthquake	24-12-2020	05-01-2021	05-01-2021	17-01-2021	IW-3/Descending	499/48	VV+VH

3.2. Seismic Events and Interferometric Pair Selection

The Himalayan region has experienced a large number of earthquakes of different magnitudes and hypocenter depths distributed from west to east. However, the primary goal of this study is to understand the impact of earthquake events on glacial deformation. Therefore, earthquakes based on the magnitude range from M_w 5.7 to M_w 4.1 with varying hypocenter depths have been selected close to Himalayan glaciers at various locations.

Seismic DInSAR studies rely on selecting optimal SLC data pairs to obtain a good-quality co-seismic deformation field. Since the analysis is based on understanding the seismic deformation of Himalayan glaciers, interferometric pairs have been selected to capture a complete seismic signal based on the following: (a) the SLC products should provide the best possible areal coverage within the influence area of an earthquake; (b) the shortest possible temporal baseline; and (c) the earliest post-seismic acquisition; (d) the maximum possible areal coverage around the epicenter location.

These criteria helped minimize decoherence, as the shortest temporal baseline ensures high coherence, especially while investigating low-latitude regions and minimizing the effect of ongoing glacial deformation after the earthquake. The influence area for each earthquake event has been determined using USGS shake maps (https://earthquake.usgs.gov/data/shakemap/). For the earthquake events devoid of shake maps, the influence area has been determined from the shake maps of other earthquakes with similar magnitude and hypocenter depths.

3.3. Vertical Displacement

SAR systems such as Sentinel-1A/B are active radar systems operating in the microwave spectrum, transmitting and receiving pulses from the Earth's surface [58]. The processing begins with identifying the primary and secondary images for DInSAR analysis, as shown in Figure 2. This involves obtaining pre-seismic SLC data as the primary file and the co-seismic data as the secondary file, respectively. The orbit state vectors were improved using precise orbit information, followed by the co-registration of primary and secondary images for the same sub-swath using 30 m Shuttle Radar Topography Mission

(SRTM) digital elevation model (DEM) [59]. Enhanced spectral diversity (ESD) was used to determine the constant azimuth offset [60].

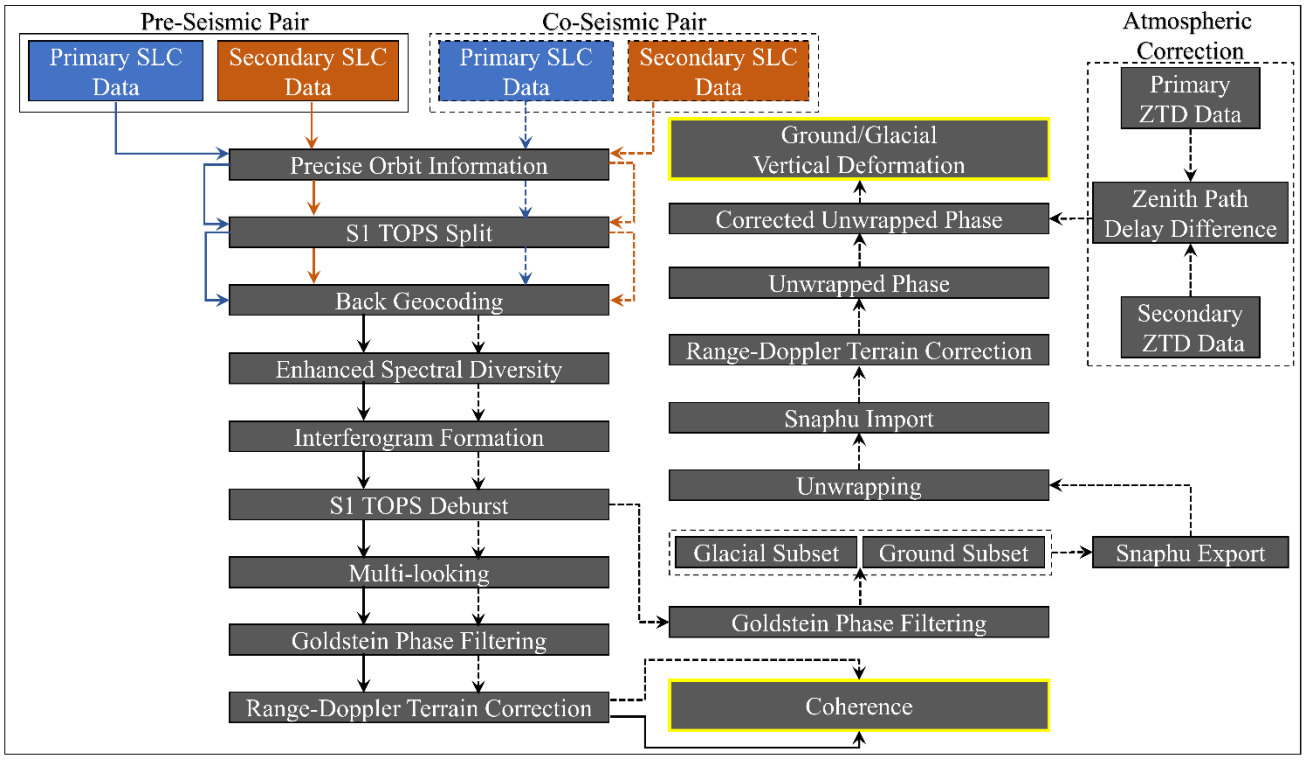


Figure 2. Process diagram for estimating atmospherically corrected vertical displacement and coherence of ground and glaciers.

Interferograms were generated through standard methods based on phase differences in data pairs. A deburst algorithm was used to integrate the interferogram into a single sub-swath product [60]. This is followed by topographic phase removal for phase flattening [61]. Goldstein phase filtering was applied to increase the signal-to-noise (SNR) ratio, thus improving the unwrapping process [62]. The flattened interferogram delivers an ambiguous estimation of the relative terrain altitude within 2π cycles of the interferometric phase. In the field of radar interferometry, the principal observation is the relative phase signal in line-of-site (LOS), depicted as the 2π modulus of the absolute phase signal [29].

Phase unwrapping is the process of adding the appropriate integer multiple of 2π to flattened interferometric fringes to produce the absolute interferometric phase information from its wrapped product lying in the range of –π to +π (ESA, 2016). Here, the phase unwrapping of the generated filtered interferogram has been performed in the statistical cost and network flow algorithm for phase unwrapping (SNAPHU) [63]. All the other processing steps have been carried out in SNAP software. Orthorectification (geocoding) of the unwrapped phase was performed using range-Doppler terrain correction [64]. Finally, the vertical displacement from the unwrapped phase has been derived using the following equation:

$$z_{vertical} = \frac{\phi_{unwrapped}\lambda_{SAR}}{-4\pi\cos\theta_{in}} \quad (1)$$

where $\phi_{unwrapped}$ represents an unwrapped phase interferogram, λ_{SAR} is the C-band wavelength of the Sentinel-1 SAR instrument (57 mm), and θ_{in} is the incident angle [65]. Division by the cosine of the incidence angle converts the line-of-sight (LOS) displacement to vertical displacement. λ_{SAR} of Sentinel-1 data is 5.56 cm and is affected by atmospheric delay, which can be corrected using zenith total delay (ZTD) maps from the generic atmospheric

correction online service for InSAR (GACOS) [66–69]. The difference in ZTD maps obtained for the primary and secondary datasets are deducted from the unwrapped phase to obtain the atmospherically corrected unwrapped phase, which is further used to derive vertical displacement.

4. Results

4.1. 2020 Tibet Earthquake, M_w 5.7

For the purpose of detecting surface deformation from an earthquake event of sufficiently high magnitude ($M_w > 5$), DInSAR is an effective approach [17]. There exists a strong correlation between the magnitude of an earthquake event and its detectability through SAR interferometry. Earthquake events with larger magnitudes create significant surficial displacement that can be captured in the interferogram, and the deformation signal generated due to high-magnitude earthquakes differs from other background processes [17]. Another critical factor is the hypocenter depth. The hypocenter depth governs whether an earthquake event of a given magnitude generates surface deformations with sufficient amplitude to be detected through DInSAR. As a general rule, the deeper the earthquake, the smaller the deformation amplitude at the Earth's surface [70]. This makes shallow seismic events more detectable through co-seismic interferograms.

In the case of the 2020 Tibet earthquake, with a hypocenter depth of 10 km, lobate deformation with a 10 km wide series of concentric fringes can be seen in the phase image, as shown in Figure 3A,D. The center of the concentric fringes represents the earthquake epicenter, which lies approximately at a distance of 13.7 km from the USGS epicenter. The vertical displacement around the epicenter lies between 0 and −168 mm. Negative displacement values indicate the subsidence at the surface, with maximum motion away from the epicenter at the DInSAR-derived epicenter location, as shown in Figure 3B,C,E,F. The wrapped and unwrapped phase information of the earthquake events, shake maps, isoseismal contours, focal mechanisms, and beach ball solutions are provided in the Supplementary Materials. For DInSAR-based seismic deformation studies, the reliability and quality of results generated from unwrapped phase information depend on the co-seismic coherence [29]. The regions of high co-seismic coherence can be considered as the regions of more reliable surface displacement. To enhance the quality of the derived results, vertical displacement of the regions having high co-seismic coherence ($\geq$0.6) has been masked out, as shown in Figure 3C,F. The influence area of the earthquake is defined from the isoseismal contours (intensity-V of the Modified Mercalli Intensity (MMI) scale) of the event shake map (https://earthquake.usgs.gov/earthquakes/eventpage/us70008cld/shakemap/intensity) and is considered as a circular area up to a distance of 69 km from the USGS epicenter. The mean vertical displacement in the region is found to be −47.3 mm. We observe that there is only subsidence due to the 2020 Tibet earthquake (M_w 5.7). Li et al. in 2022 detected the co-seismic deformation for the Tibet earthquake using ISCE (InSAR Scientific Computing Environment) [71] with maximum amplitude on the order of −126 and −157 mm through ascending and descending tracks, respectively. A seismogenic fault (dipping northeast) was detected with the main rupture zone of ~5 × 5 km^2 and maximum co-seismic quasi-vertical displacement of −164 mm. In Figure 4A, we show the difference in pre- and post-seismic coherence, computed as outlined by Fielding and Jung in 2024 [72]. This difference can be used as a proxy for locations of significant change in surface properties, such as damage, vegetation, or water content, over that time period. Figure 4B represents the vertical displacement of the glacial bodies ranging between 0 and −79 mm with a mean displacement of −38.9 mm. To check for variation in surficial features such as glacial moraine deposits around the glacial bodies, the changes in coherence due to earthquake events were calculated, as shown in Figure 4A. A reduction in the coherence can be observed from

pre-seismic to co-seismic pairs in some of the regions around the earthquake epicenter within the lacustrine deposits of natural lakes (Lake Dingmu) and human settlements [31]. Reduced coherence can be seen around some glacial bodies. However, such changes are not significant in the glacial bodies close to the periphery of the influence area, which is quite far away from the epicenter of the earthquake.

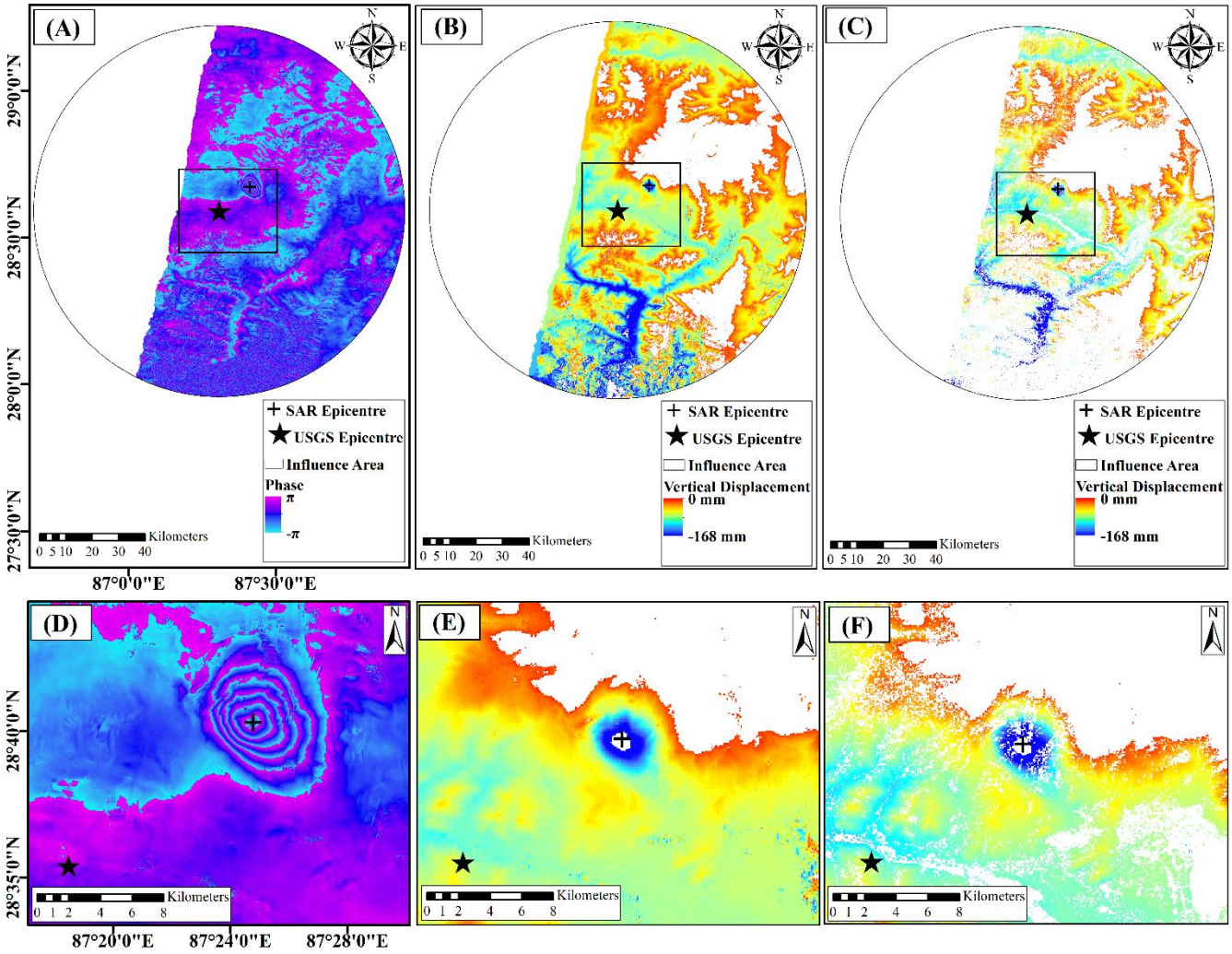


Figure 3. Map for 2020 Tibet earthquake (M_W 5.7) showing (**A**) orthorectified phase interferogram, (**B**) vertical displacement, (**C**) vertical displacement for coherence $\geq$ 0.6, co-seismic image, (**D**) orthorectified phase interferogram at epicenter location, (**E**) vertical displacement at epicenter location, and (**F**) vertical displacement for coherence $\geq$ 0.6, co-seismic image.

4.2. 2020 Leh Earthquake, M_w 5.3, and 2017 Thang Earthquake, M_w 5.2

Figure 5 shows the vertical displacement captured due to the 2020 Leh earthquake (M_w 5.3). Within the influence radius of 61 km, vertical displacement lies between 31 mm and −33 mm. Unlike the 2020 Tibet earthquake, where there is no uplift after the earthquake, only subsidence, regions close to the epicenter of the 2020 Leh earthquake show positive vertical displacement and negative vertical displacements moving away from the epicenter. For the areas with coherence $\geq$0.6, the mean vertical displacement is found to be −2.4 mm. Figure 6A shows the coherence change obtained by subtracting pre-seismic coherence values from the co-seismic coherence values. Reduction in coherence can be observed around the glacial bodies. Even though surface deformations can be the primary source of decorrelation, other factors such as decorrelation due to sensor noise from the radar system, geometric decorrelation due to perpendicular baseline component, and temporal

decorrelation due to changes in surficial features and/or vegetation are important [31,73]. Thus, temporal decorrelation before and during an earthquake event may, in part, be the result of surficial changes and/or changes in vegetation cover. As Leh is characterized as a high-altitude dry–cold mountainous desert [74], such reduced coherence due to an earthquake event around glacial bodies can indicate the deformation/alteration of glacial moraines. However, because of the shape and size of the glacial bodies, it is difficult to unwrap glacial subset regions. Figure 6B represents the displacement of glacial bodies (obtained from the unwrapped phase information for the entire sub-swath), where the glaciers lying close to the epicenter show positive displacement or uplift. The glacial bodies far from the epicenter capture subsidence. The mean vertical displacement of glaciers is found to be −2.5 mm. However, with an influence radius of 61 km, the region of investigation for seismic deformation is large and consists of ground surface and glacial bodies, which are quite different from each other in terms of their material properties. Unwrapping the DInSAR phase information for the entire influence area of the earthquake may introduce unwrapping errors. Therefore, we investigated the vertical displacement due to seismic events and the surrounding ground surface separately to avoid any unwrapping errors while considering a larger area. Considering small patches of glaciated regions and ground surface separately (Figure 7) at an almost equal radial distance of 41 km shows that the glacial region experiences negative vertical displacements of up to −78 mm, which is much greater than the ground displacement, which lies in the range of 18 mm and −32 mm. The vertical ground displacement shown in the sub region of Figure 7C lies within the range of seismic displacement shown in Figure 5B. Moreover, where the ground surface shows both uplift and subsidence, the glacial patch shows only subsidence. One possible reason for the differences in the seismic deformation of glacial bodies and the ground surface could be related to their different rheologies, material properties, and dynamic response. Glaciers are huge masses of metamorphosed ice that behave as a Kelvin Voight (non-Newtonian) material with the ability to flow, unlike the elastic Earth's crust [75]. As a result, the impact of earthquakes on glacial bodies will be different from that of the ground surface.

For the 2017 Thang earthquake (M_w 5.2), the vertical displacement ranges between 51 mm and −39 mm within the influence radius of 56 km, with the mean displacement of 2.8 mm for regions masked with coherence $\geq$ 0.6, as shown in Figure 8B. For the glacial bodies within the influence area, a mean vertical displacement of 3.4 mm is observed (Figure 9B). From the coherence difference map (Figure 9A), reduced co-seismic coherence can be seen within and around the glacial bodies in the influence area. Like Leh, Thang is a dry–cold mountain desert devoid of vegetation around the glaciated regions. Reduced coherence due to a seismic event within and around glacial bodies suggests surficial changes in glacial moraine deposits from that earthquake. Figure 10 shows the vertical displacement derived for glacial and ground patches separately. The glacial patches show very high vertical displacement due to the 2017 Thang earthquake that reaches up to −173 mm and −576 mm, as shown in Figure 10B and 10C, respectively, while the seismic displacement of the solid earth patches does not exceed −39 mm. This also is observed for the entire seismic displacement influence area, as shown in Figure 8. It also is interesting to observe that the glacial patch farther from the epicenter and surrounded by larger glacial bodies shows larger vertical displacement (Figure 10C) than the glacial patch close to the epicenter (Figure 10B). One possibility could be the site-specific amplification of the seismic waves, which is probably dependent on the material properties of glacial bodies, including the shear modulus, damping coefficient, and thickness. However, a better understanding of these effects would require extensive field- and lab-based studies of the behavior of glacial ice under seismic loading.

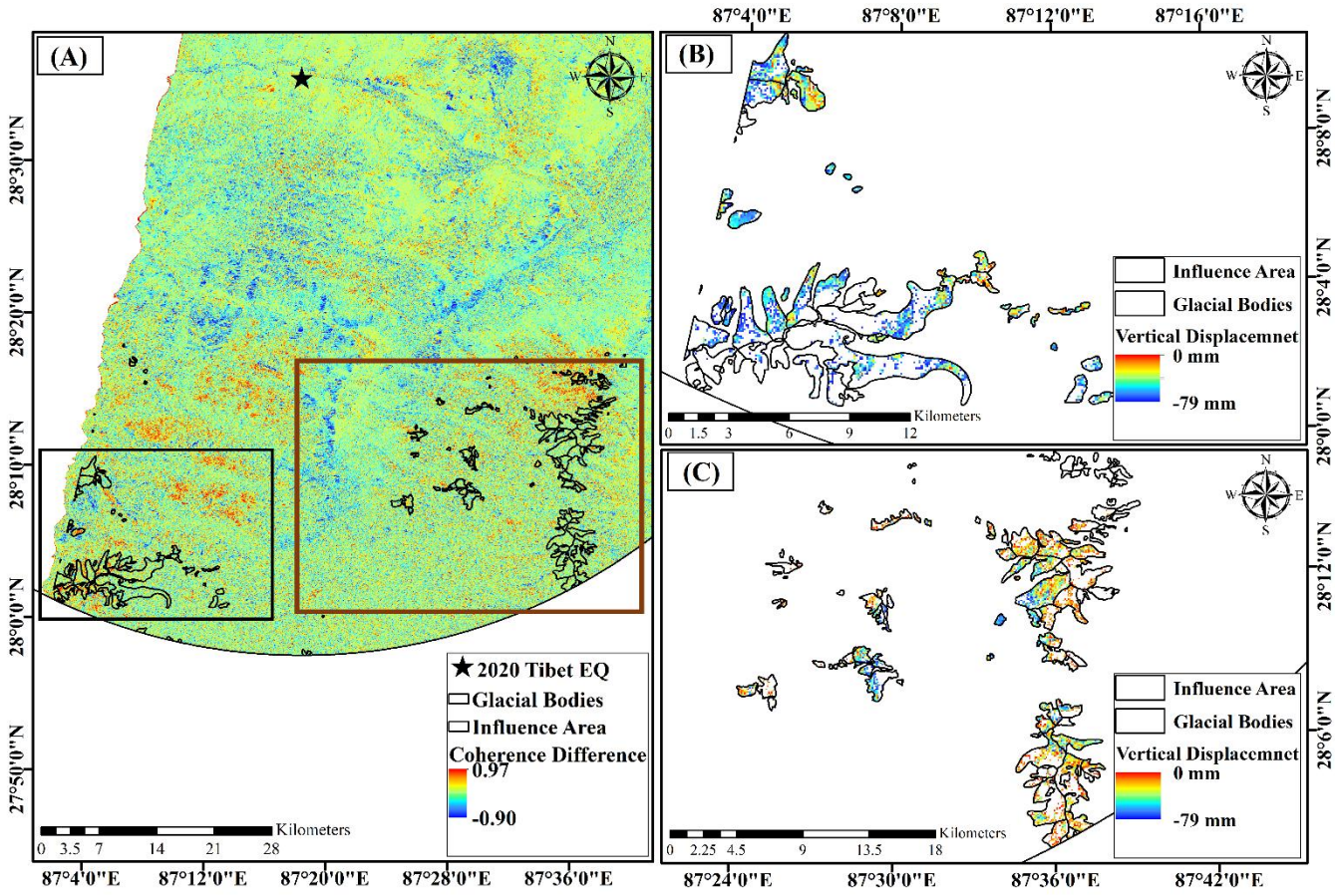


Figure 4. Map showing orthorectified layer of (**A**) difference between pre- and co-seismic coherence, (**B**,**C**) vertical displacement (mm) within glacial bodies derived from unwrapped phase interferogram for 2020 Tibet earthquake (M_w 5.7) within black and brown rectangular regions, respectively.

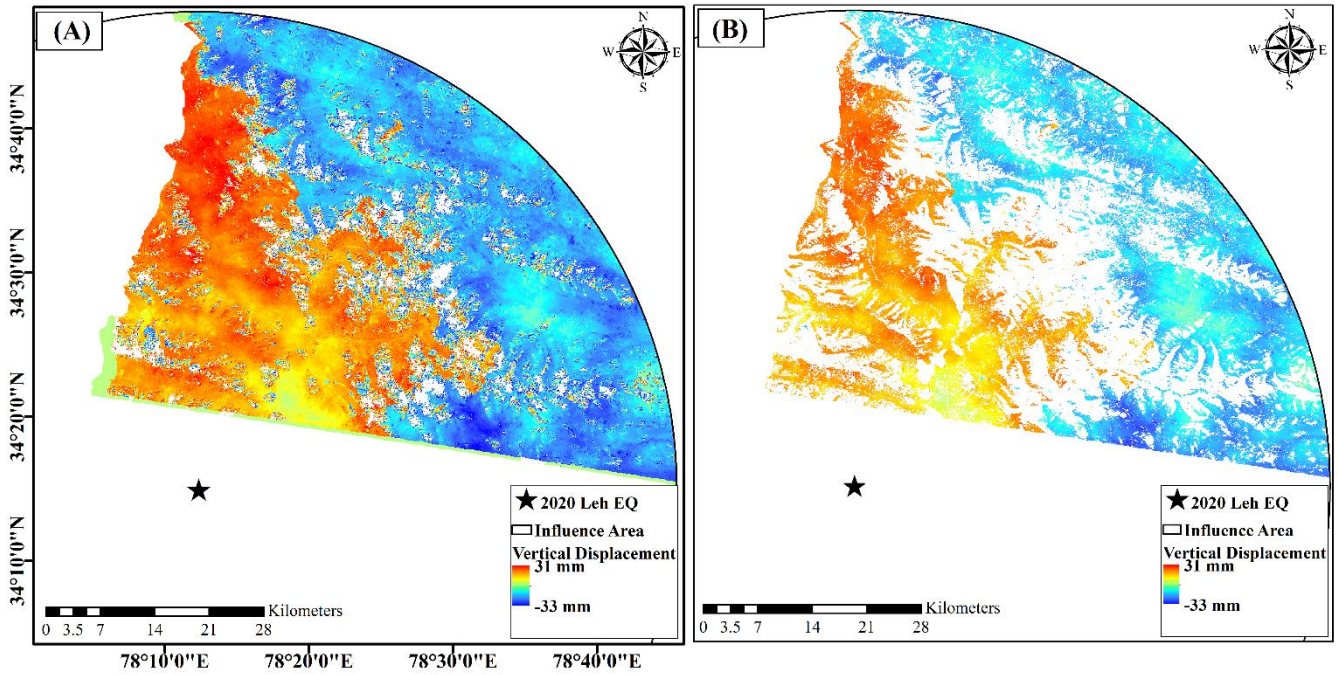


Figure 5. Map showing (**A**) orthorectified vertical displacement and (**B**) vertical displacement with co-seismic coherence $\geq$ 0.6 for 2020 Leh earthquake (M_w 5.3).

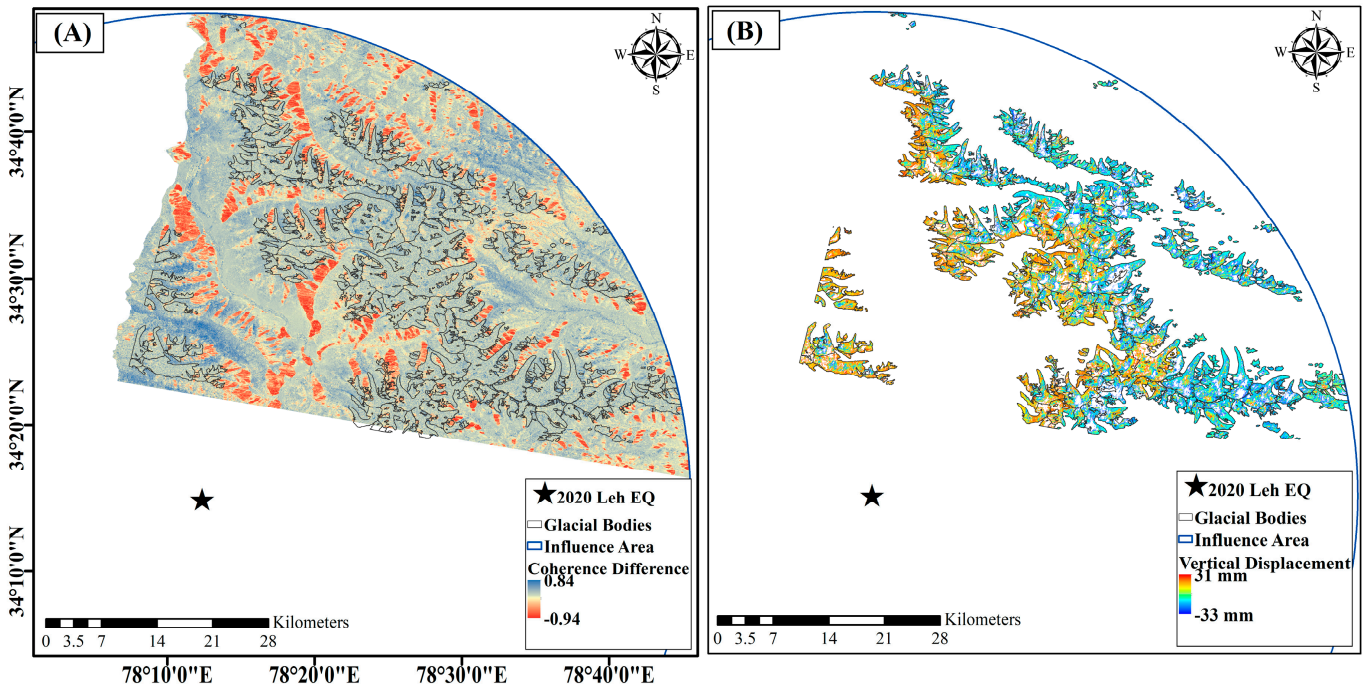


Figure 6. Map showing (**A**) difference between pre- and co-seismic coherence and (**B**) vertical displacement (mm) within glacial bodies derived from unwrapped phase interferogram for 2020 Leh earthquake (M_w 5.3).

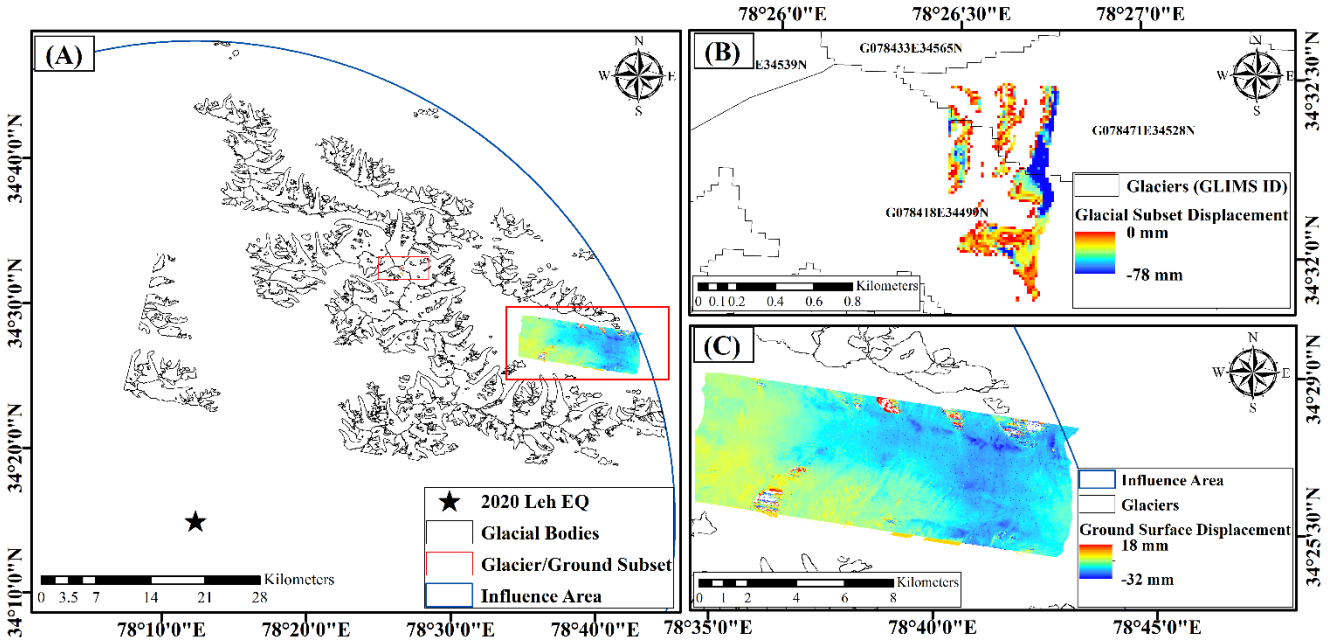


Figure 7. Map showing (**A**) glacial and ground subset regions, (**B**) vertical displacement (mm) within glacial subset, and (**C**) vertical displacement (mm) within ground subset derived from unwrapped phase interferogram for 2020 Leh earthquake (M_w 5.3).

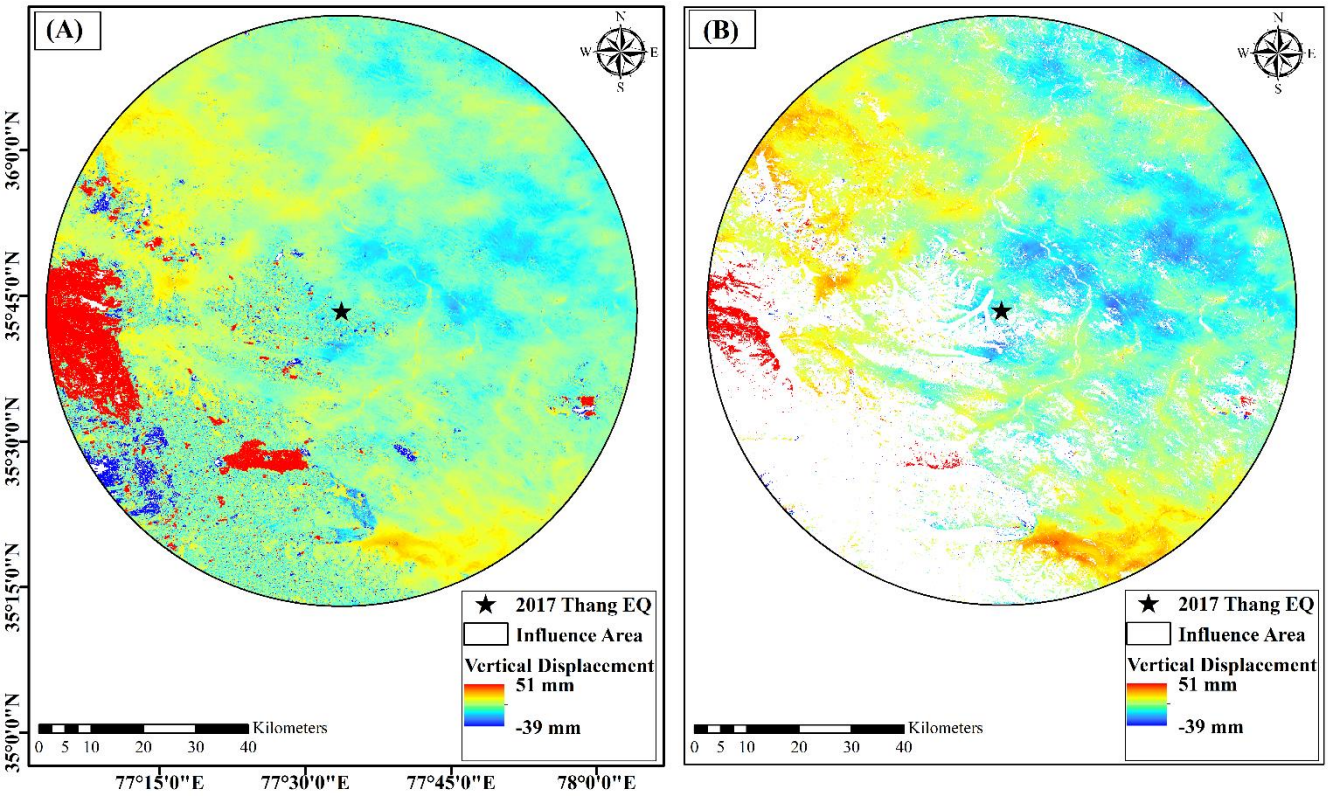


Figure 8. Map showing (**A**) orthorectified vertical displacement and (**B**) vertical displacement with co-seismic coherence $\geq$ 0.6 for 2017 Thang earthquake (M_w 5.2).

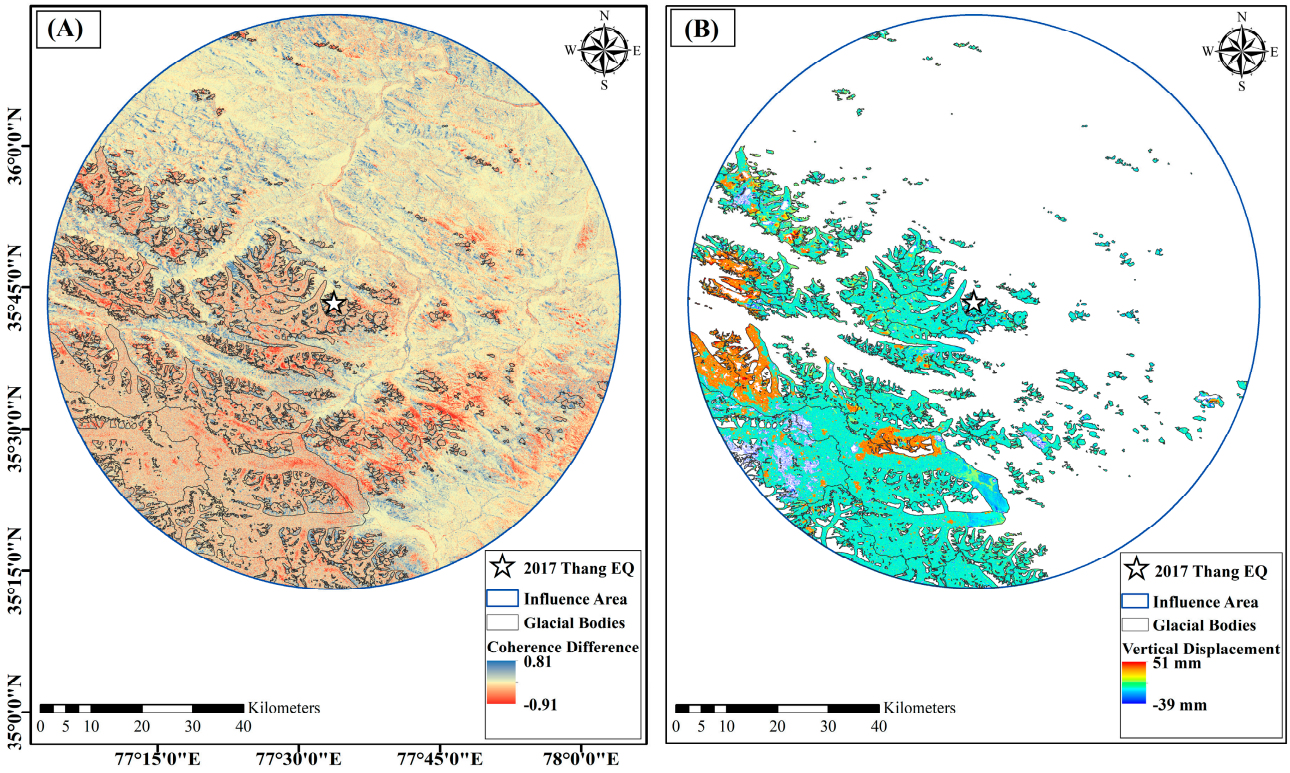


Figure 9. Map showing (**A**) difference between pre- and co-seismic coherence and (**B**) vertical displacement (mm) within glacial bodies derived from unwrapped phase interferogram for 2017 Thang earthquake (M_w 5.2).

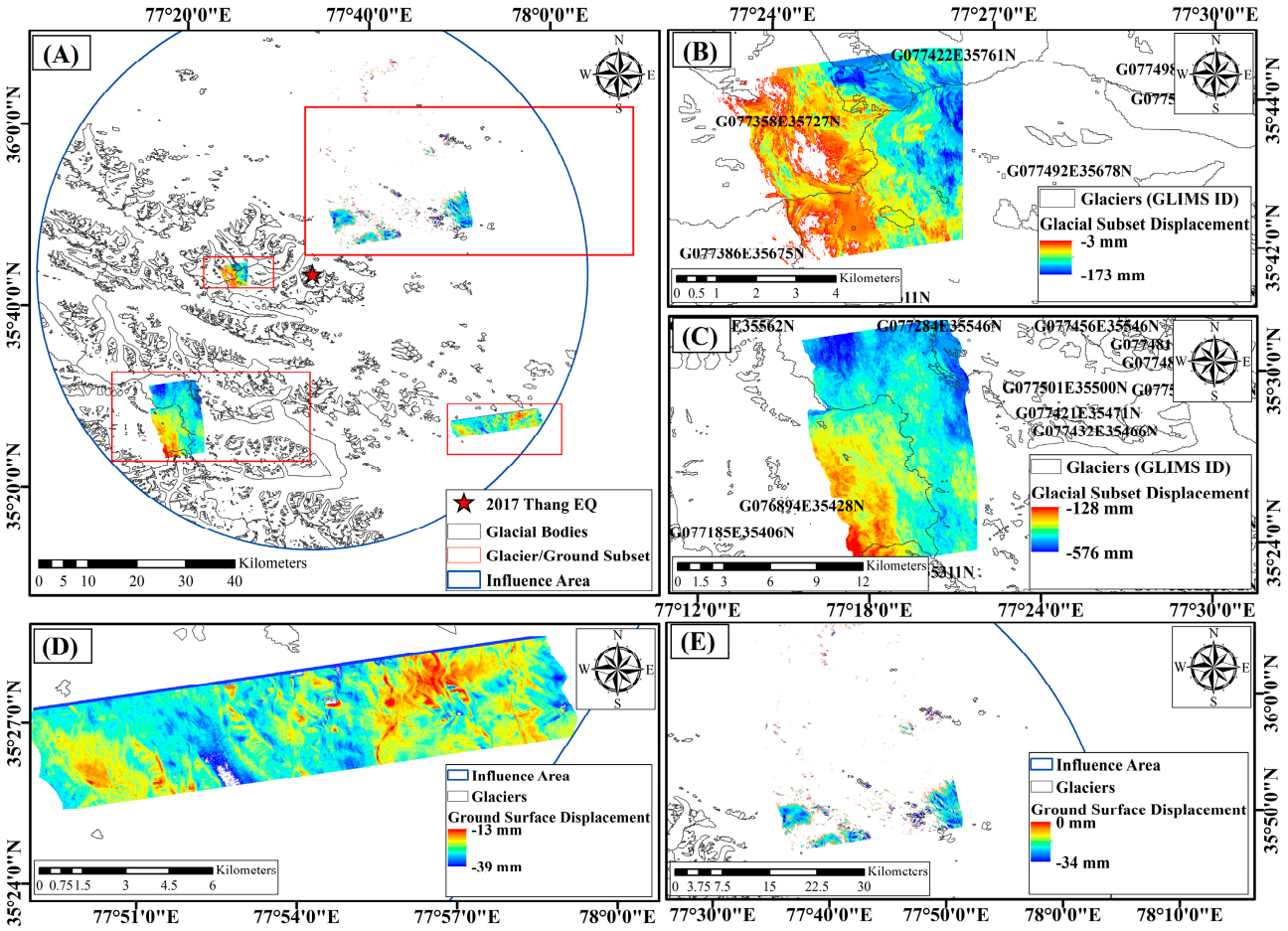


Figure 10. Map showing (**A**) glacial and ground subset regions, (**B**) vertical displacement (mm) within glacial subset-I, (**C**) vertical displacement (mm) within glacial subset-II, (**D**) vertical displacement (mm) within ground subset-I, and (**E**) vertical displacement (mm) within ground subset-II.

4.3. 2021 Joshimath Earthquakes, M_w 4.5

The Joshimath earthquake (M_w 4.5) occurred on 23 May 2021 at a hypocentral depth of 10 km near the Gangotri glacier. Figure 11 shows the vertical displacement of the Earth's surface within the influence area (54 km). The earthquake resulted in both uplift and subsidence, in the range of 45 mm and −52 mm, respectively. Earthquake-induced vertical displacement for the regions with co-seismic coherence ≥ 0.6 shows a mean vertical displacement of approximately 0.64 mm. For the glacial bodies, a mean vertical displacement of −2.2 mm is observed (Figure 12C,E). A major region within the influence area shows negative vertical displacement, with the exception of some small patches and the northeastern region of the influence area. The majority of glacial bodies are situated in the east–west region and very few in the northern side of the influence area. Therefore, the mean vertical displacement of the glacial bodies shows slightly greater subsidence compared to the mean vertical displacement of the ground surface within the influence area. From the coherence difference map of the influence area, a reduction in the co-seismic coherence can be observed around the glaciated regions along the northern–eastern side of the influence area where earthquake-induced uplift is observed. Figure 13 shows the seismic displacement of glacial and solid earth patches. As was observed for the 2020 Leh earthquake and 2017 Thang earthquake, the glacial patch shows seismic displacement of up to −94 mm due to the 2021 Joshimath earthquake, which is much higher than the vertical displacement of the ground patch by as much as −51 mm.

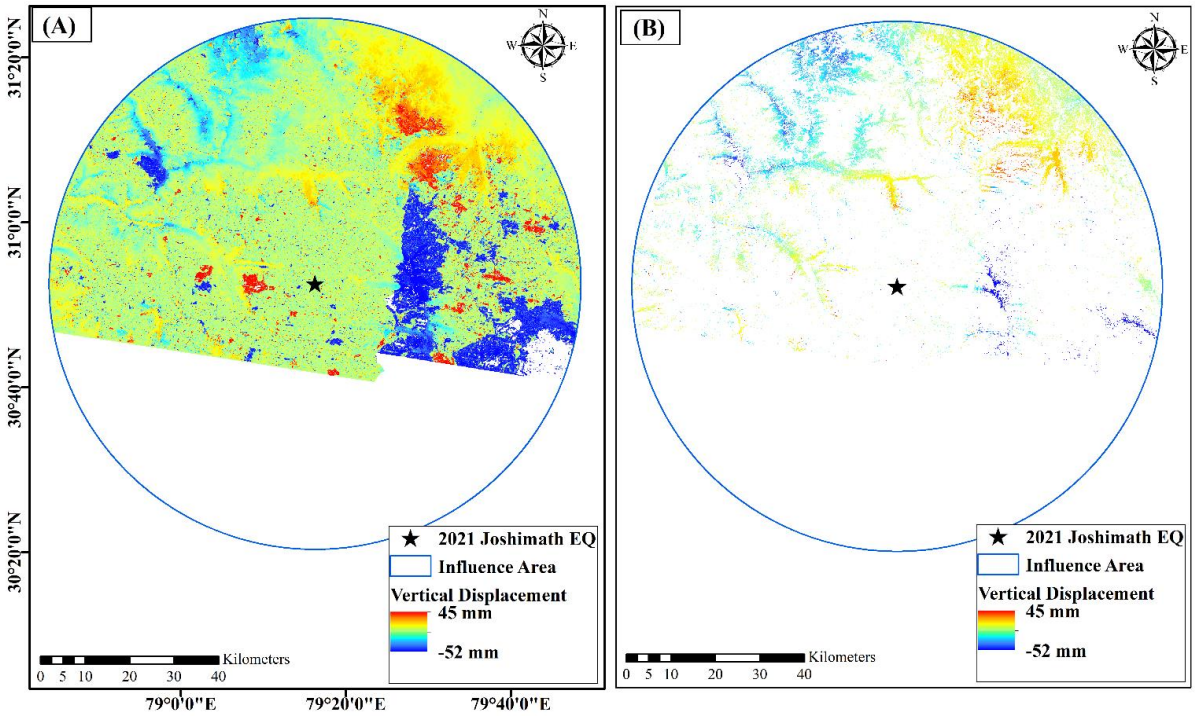


Figure 11. Map showing (**A**) orthorectified vertical displacement and (**B**) vertical displacement with co-seismic coherence $\geq$ 0.6 for 2021 Joshimath earthquake (M_W 4.5).

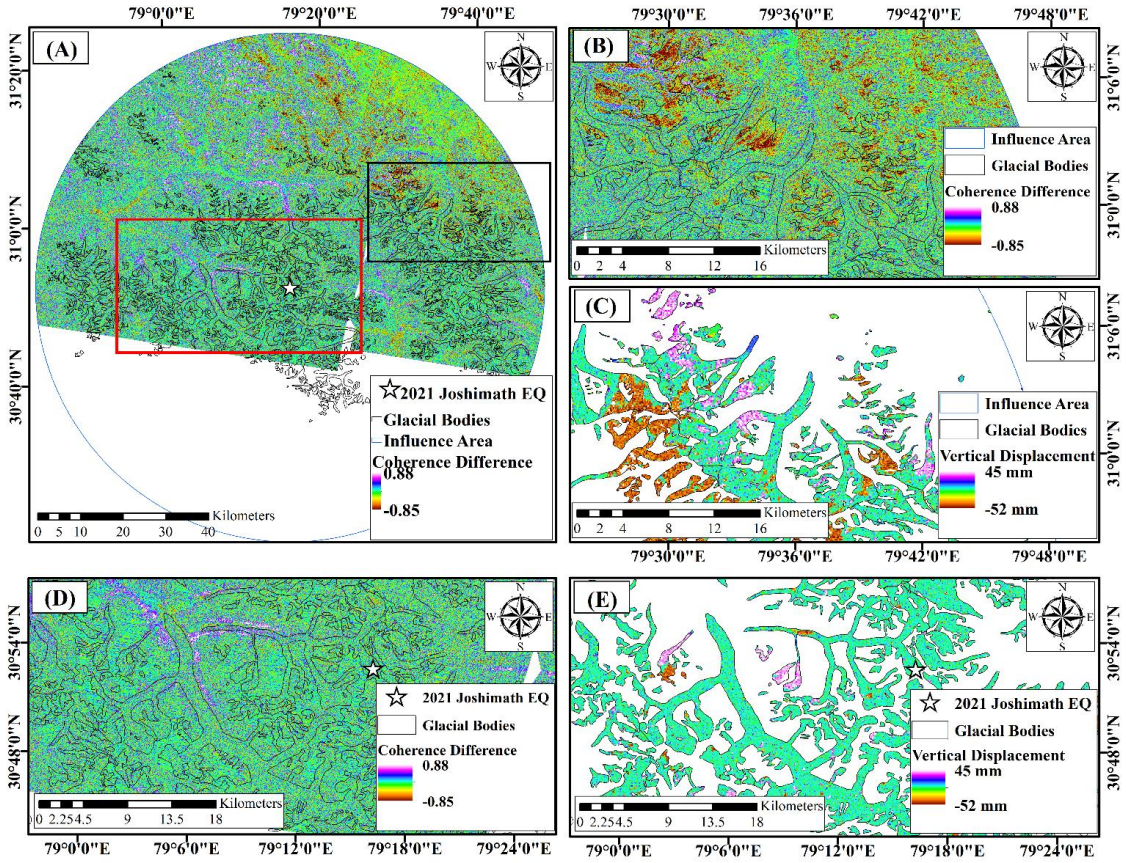


Figure 12. Map showing (**A**,**B**,**D**) difference between pre- and co-seismic coherence within the influence area, black and red rectangular regions, respectively, and (**C**,**E**) vertical displacement (mm) within glacial bodies derived from unwrapped phase interferogram for 2021 Joshimath earthquake (M_W 4.5) for black and red rectangular regions, respectively.

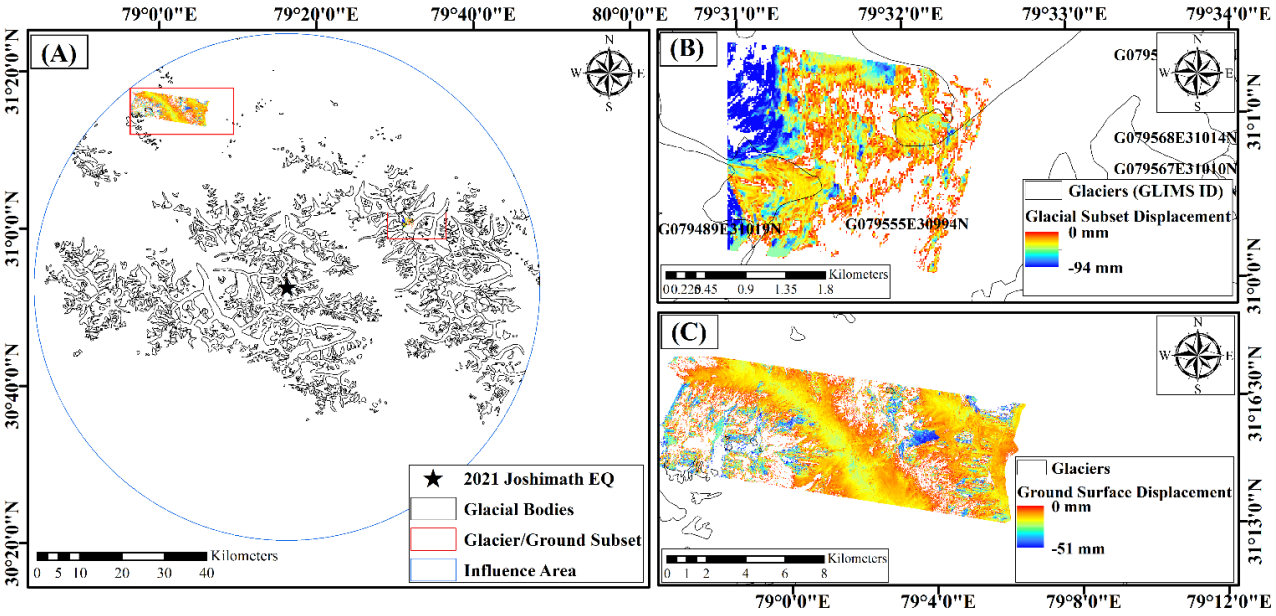


Figure 13. Map showing (**A**) glacial and ground subset regions, (**B**) vertical displacement (mm) within glacial subset, and (**C**) vertical displacement (mm) within ground subset derived from unwrapped phase interferogram for 2021 Joshimath earthquake (M_w 4.5).

4.4. 2018 Sikkim Earthquake, M_w 4.4, and 2017 Sikkim Earthquake, M_w 4.2

Sikkim is a northeastern state of India that encompasses the eastern Himalayas and is situated in the high-seismic-hazard territory (Zone-IV) [76]. Sikkim has experienced moderate seismic impacts in the past. However, shake maps are not available for the earthquake events of $M_w < 4.5$ within the northeastern Himalayan region. Thus, determining the influence radius of earthquakes is more difficult for lower-magnitude earthquakes due to a lack of isoseismal contours.

As we know, the higher the magnitude (M_w), the greater the surface deformation that can be detected in an interferogram [17]. Also, the higher the hypocenter depth (D_H), the smaller the deformation amplitude at the surface [70]. This is well represented through isoseismal contours which govern the influence radius (*IR*) of an earthquake event in terms of surface deformations. Therefore, the relationship of M_w and D_H with *IR* can be represented as Equation (2) and Equation (3), respectively.

$$M_w \propto IR \tag{2}$$

$$D_H \propto \frac{1}{IR} \tag{3}$$

The detection of earthquake impacts on the Earth's surface depends on two major parameters, which are magnitude and hypocenter depth. The 2017 Sikkim earthquake is triggered at a hypocenter depth of 10 km. In the previous sections, we investigated three other earthquake events of similar hypocenter depth but varying magnitudes, as shown in Table 3. The influence radius of these earthquakes differs linearly, as shown in Figure 14A. Thus, the influence radius of the 2017 Sikkim earthquake is calculated as 46 km. For the 2018 Sikkim earthquake, the scenario is slightly different. The earthquake was triggered at a hypocentral depth of 49.8 km. From past records, earthquakes at that hypocentral depth have not occurred in the Indian subcontinent. Thus, earthquakes of different magnitudes and hypocentral depths close to 49.8 km were considered, and their influence radii were determined from USGS shake maps, as shown in Table 3. However, their relation (*IR* vs.

M_w) is not linear. Therefore, the normalized influence radius (IR_N) for these earthquake events at a hypocenter depth of 49.8 km has been computed using Equation (4).

$$IR_N = \frac{D_H}{D_{H'}} \times IR \quad (4)$$

Here, $D_{H'}$ represents the hypocenter depth of the 2018 Sikkim earthquake from which the IR_N of each earthquake is calculated. A linear relationship exists between IR and M_w, as shown in Figure 14B. From this, the normalized influence radius of the 2018 Sikkim earthquake is computed as 17 km.

Table 3. Earthquakes and their respective magnitudes and influence radii.

Earthquakes with Hypocenter Depth of 10 km			
Event/Date	**M_w**	**IR (km)**	
Tibet Earthquake/20 March 2020	5.7	69	
Leh Earthquake/25 Sept 2020	5.3	61	
Joshirmath Earthquake/23 May 2021	4.5	54	
Sikkim Earthquake/16 May 2017	4.2	46	
Nepal Earthquake/8 November 2020	4.1	39	
Earthquakes with varying hypocenter depth close to 49.8 km			
Event/Date	**M_w**	**D_H (km)/IR (km)**	**$D_{H'}$ (km)/IR_N (km)**
Bhutan Earthquake/25 March 2003	5.5	47.1/43	49.8/41
Jaisalmer Earthquake/9 April 2009	5.1	44.3/40	49.8/34
Khangah Dogran Earthquake/19 October 2000	4.9	47.7/26	49.8/25
Sikkim Earthquake/17 June 2018	4.4	49.8/NA	49.8/17

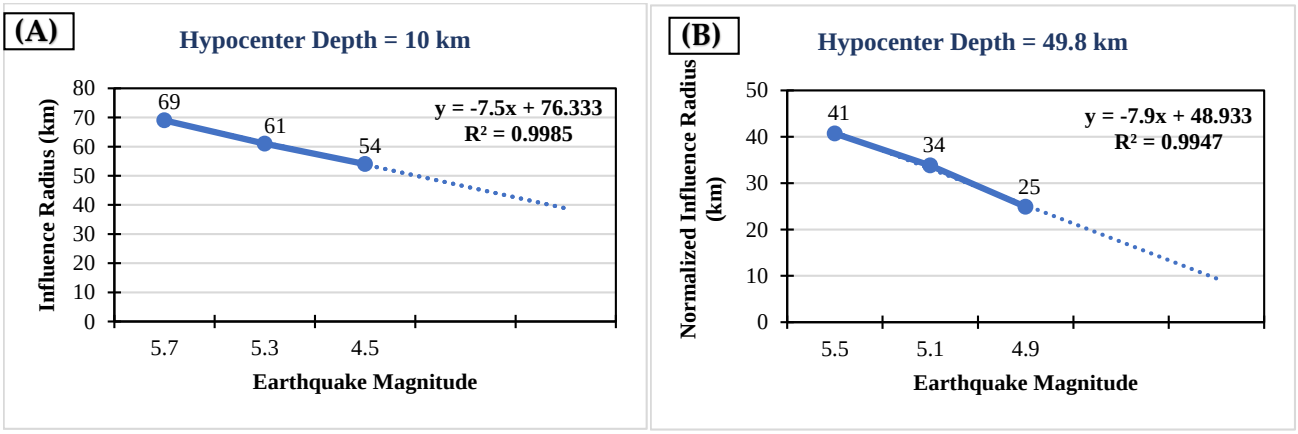


Figure 14. Relation between (**A**) IR and M_w of earthquakes triggered at hypocenter depth of 10 km and relation between (**B**) IR_N and M_w of earthquakes triggered close to hypocenter depth of 49.8 km.

Figure 15A shows the impact of the 2017 Sikkim earthquake (M_w 4.2) with a hypocenter depth of 10 km in terms of the coherence difference between pre- and co-seismic pairs. A significant reduction in co-seismic coherence has not been observed within the influence area (46 km). However, this is expected, as an earthquake event of a lower magnitude ($M_w < 4.5$) does not deliver a substantial impact on the Earth's surface [77,78]. The vertical displacement lies in the range of 0 to −19 mm, indicating subsidence, much less than the earthquake events of higher magnitudes ($M_w \geq 4.5$) discussed in the previous sections. The earthquake-induced vertical displacements do not propagate to the glacial bodies which are clustered in the influence area's northern region. Figure 16 shows the coherence difference map of the 2018 Sikkim earthquake (M_w 4.4) triggered at a hypocenter depth of 49.8 km. The earthquake results in negligible impact within the influence area of 17 km. Where the epicenters of the 2017 and 2018 earthquake events lie within Sikkim at a distance of 31.7 km

from each other, the 2017 earthquake (M_w 4.2) shows some subsidence, whereas vertical displacement has not been captured for the 2018 earthquake. The earthquake that occurred in 2017 is comparatively shallow. DInSAR-based detectable surficial displacement due to a deeper earthquake is smaller than a shallow earthquake of the same magnitude. To better understand the impact of moderate earthquake events of the same magnitude but with different hypocentral depths on glacial bodies, two different earthquake events in the Nepal region are investigated in the next section.

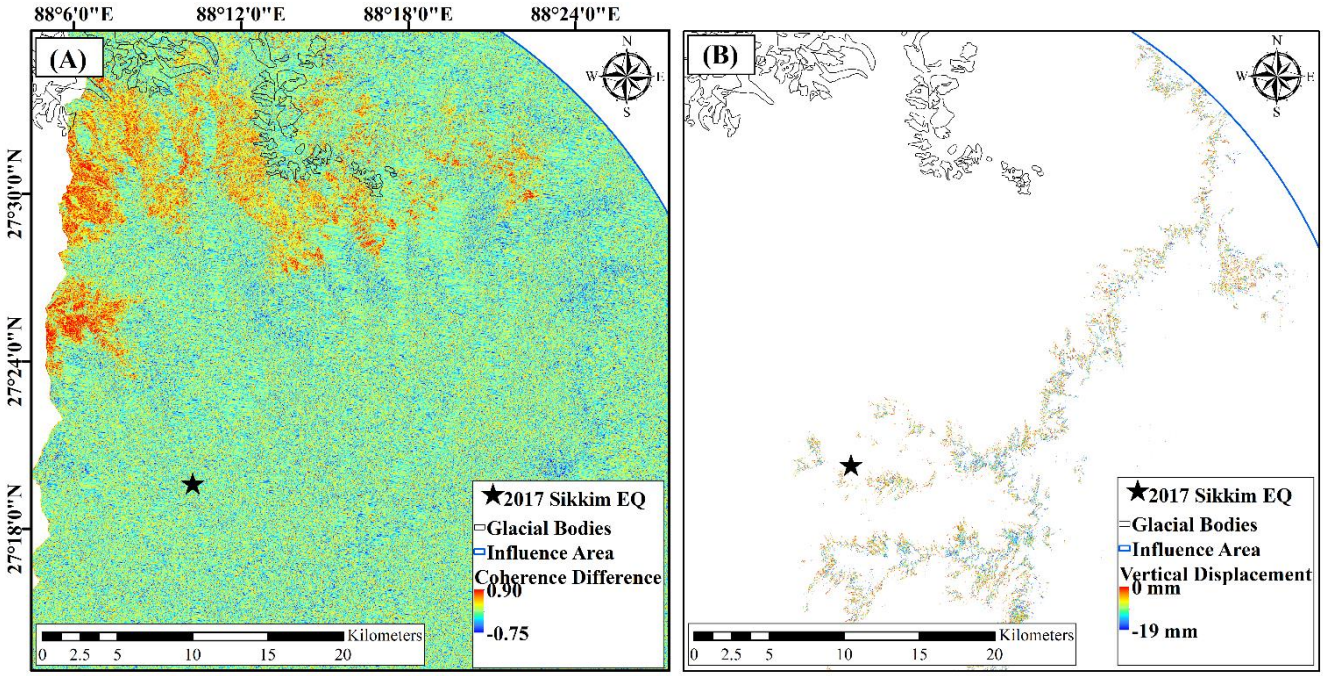


Figure 15. Map showing (**A**) difference between pre- and co-seismic coherence and (**B**) vertical displacement (mm) within influence area derived from unwrapped phase interferogram for 2017 Sikkim earthquake (M_w 4.2).

4.5. Nepal Earthquakes in 2020 and 2021, M_w 4.1

The comparative study of the impact of earthquakes on glacial bodies is a challenging task, as it is rare for two earthquake events of similar magnitude to occur at exactly the same location. Even if two seismic events of similar magnitude occur in the proximity of glacial bodies, hypocenteral depth and distance from the glacial bodies govern the magnitude of the vertical displacement. This section attempts to understand the vertical displacement within glacial bodies due to two different earthquake events of M_w 4.1 triggered at a similar distance from the glacial bodies but with different hypocenter depths. Despite having similar magnitudes, the influence radius of both earthquakes is different due to the change in depth. The influence radius of the 2020 Nepal earthquake, at a hypocentral depth of 10 km, is computed as 39 km (Table 3). For the 2021 Nepal earthquake, with a hypocentral depth of 35 Km, previous records of earthquake events and their respective shake maps have been utilized to derive the normalized influence radius of 34 km, as shown in Table 4. The linear relationship between the normalized influence radius of earthquakes and their magnitudes is shown in Figure 17.

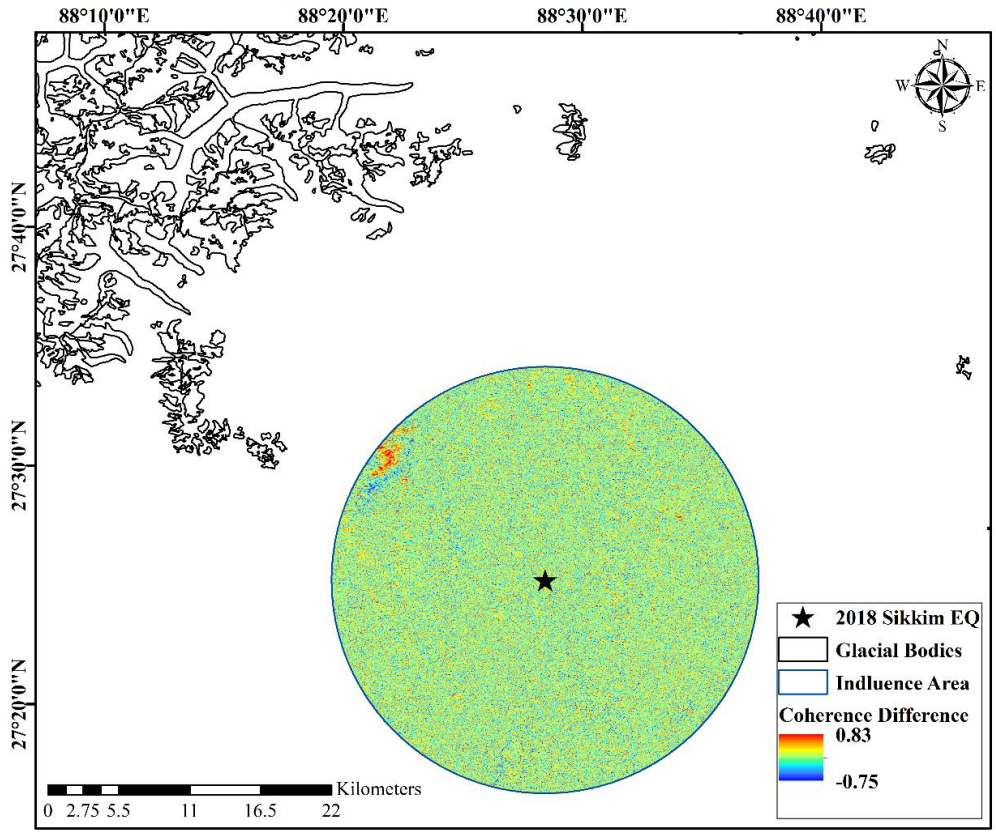


Figure 16. Map showing difference between pre- and co-seismic coherence for 2018 Sikkim earthquake (M_W 4.4).

Table 4. Earthquakes and their respective magnitudes and influence radii close to a hypocenter depth of 35 km.

Earthquakes with Varying Hypocenter Depth Close to 35 km			
Event/Date	**M_w**	**D_H (km)/IR (km)**	**$D_{H'}$ (km)/IR_N (km)**
Dhekiajuli Earthquake/28 April 2021	6.0	34/71	35/70
Haripur Earthquake/10 October 2010	5.2	33.2/60	35/57
Bageshwar Earthquake/1 May 2010	4.5	35.5/45	35/46
Nepal Earthquake/11 January 2021	4.1	35/NA	35/34

The 2020 Nepal earthquake resulted in a vertical displacement of between 0 to −16 mm, indicating surface subsidence (Figure 18B). The mean displacement is −10 mm. Within the glacial bodies, the mean vertical sinking is 7.7 mm. On the other hand, the 2021 earthquake resulted in a vertical displacement in the range of 0 to −12 mm with a mean displacement of −5.4 mm, as shown in Figure 19B–D. The earthquake events occurred at a distance of 33 km from each other in the winter of 2020–2021 (within 64 days). A common circular study zone, considering the distance between the two event epicenters as the diameter, is demarcated to capture the vertical displacements of two earthquake events of the same magnitude but with different hypocenter depths positioned at the same distance from common glacial bodies. The 2020 earthquake, at a comparatively shallow depth, shows a much larger region of subsidence in the glacier than the 2021 earthquake (Figure 20). As energy dissipation is greater for an earthquake of greater hypocentral depth, shallow earthquakes deliver more impact on the surface. Figures 18A and 19A show the coherence difference map of the 2020 and 2021 earthquakes, respectively. Significant changes in coherence have not been observed in either case. Even though some locations show reduced co-seismic coherence

values, this can be attributed to changes due to other factors. As vegetation cover surrounds the region, as shown in the false-color-composite (FCC) map (Figure 21), the coherence difference can be attributed to changes in vegetation cover.

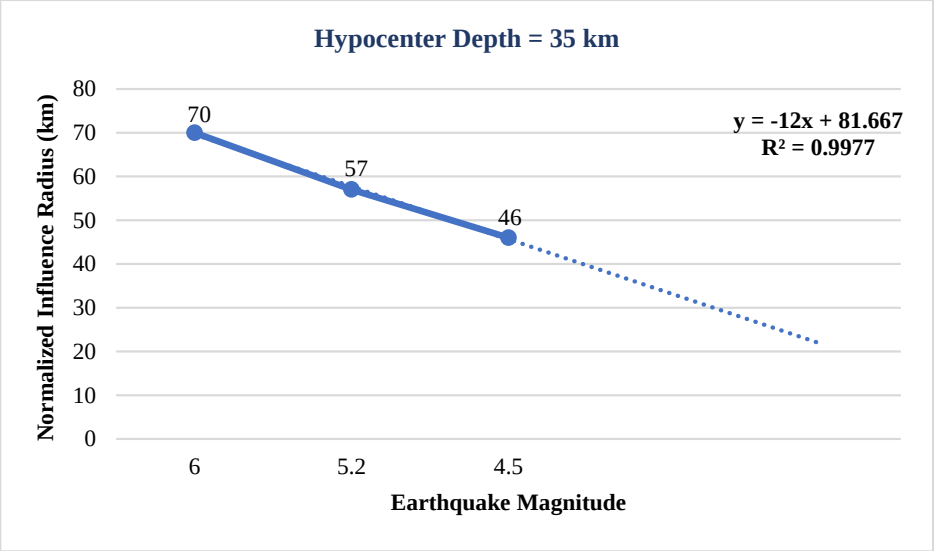


Figure 17. Relation between IRN and M_w of earthquakes triggered close to hypocenter depth of 35 km.

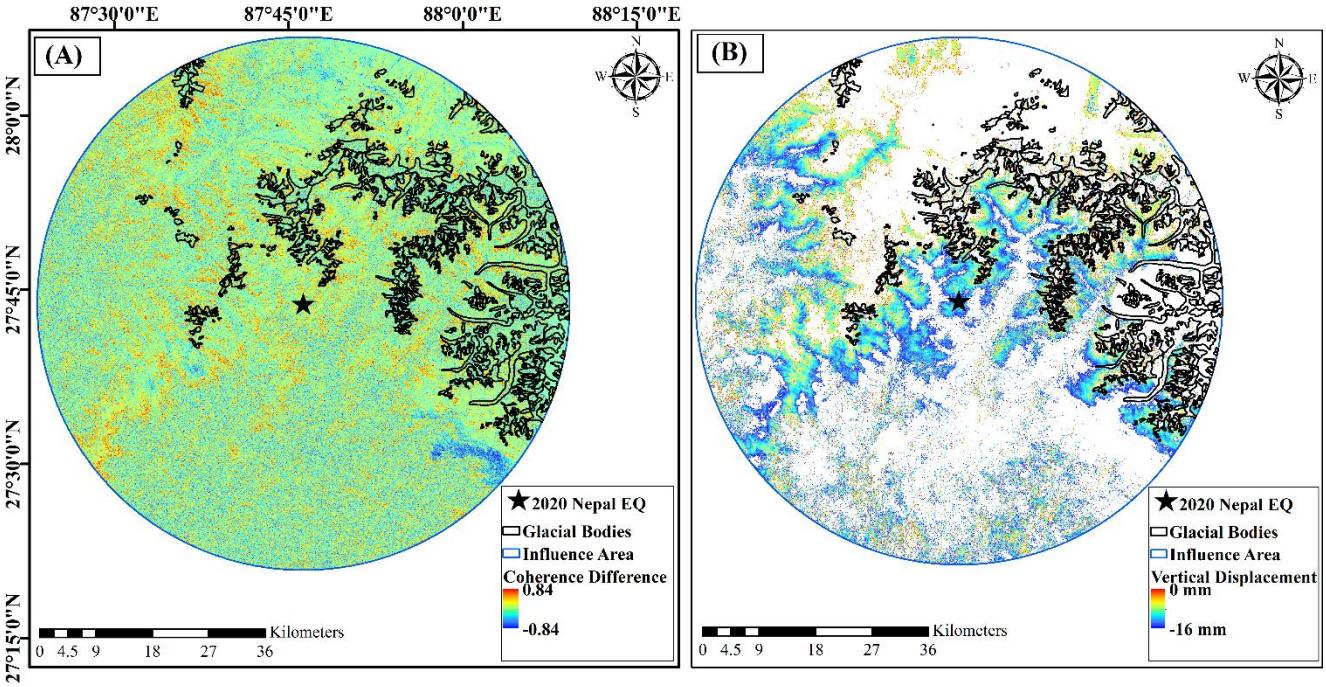


Figure 18. Map showing (**A**) difference between pre- and co-seismic coherence and (**B**) vertical displacement (mm) within an influence area derived from unwrapped phase interferogram for 2020 Nepal earthquake (M_w 4.1).

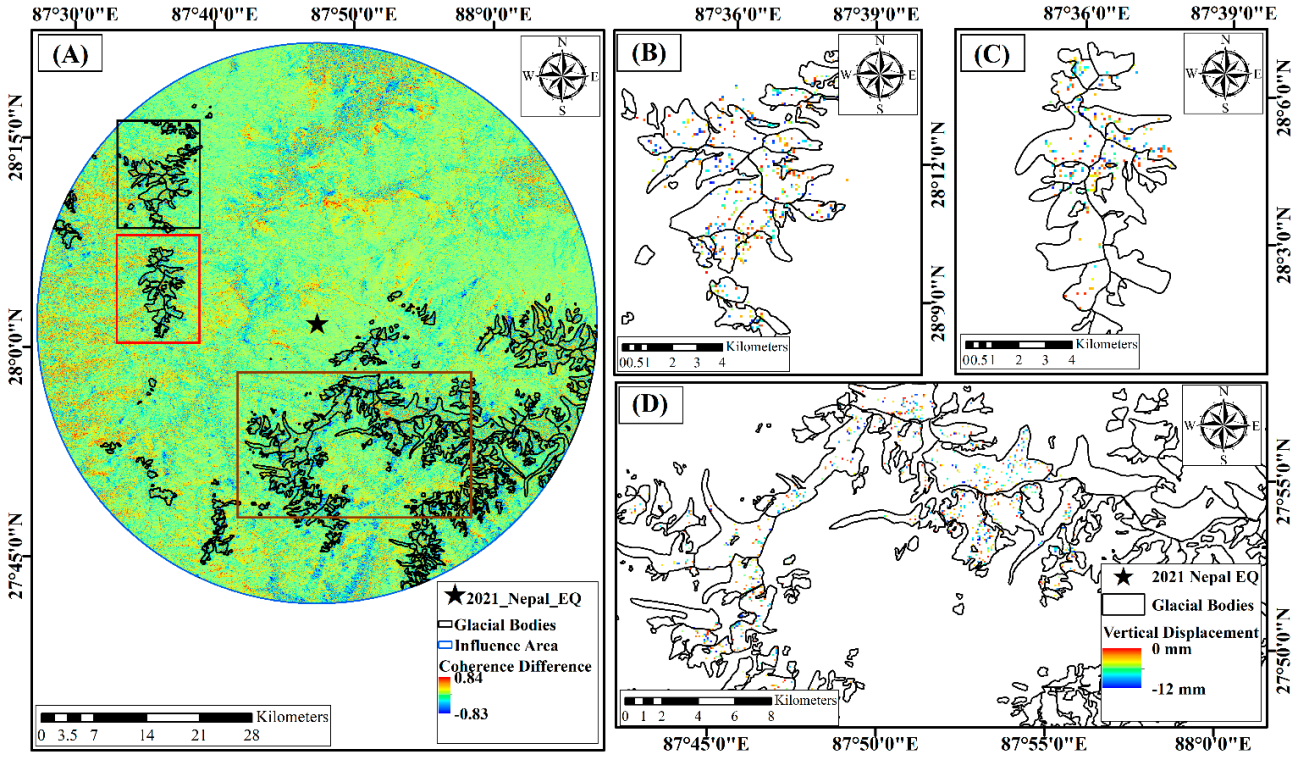


Figure 19. Map showing (**A**) difference between pre- and co-seismic coherence and (**B**–**D**) vertical displace-ment (mm) within influence area (in red, black and brown frames respectively) derived from un-wrapped phase interferogram for 2021 Nepal earthquake (M_W 4.1)

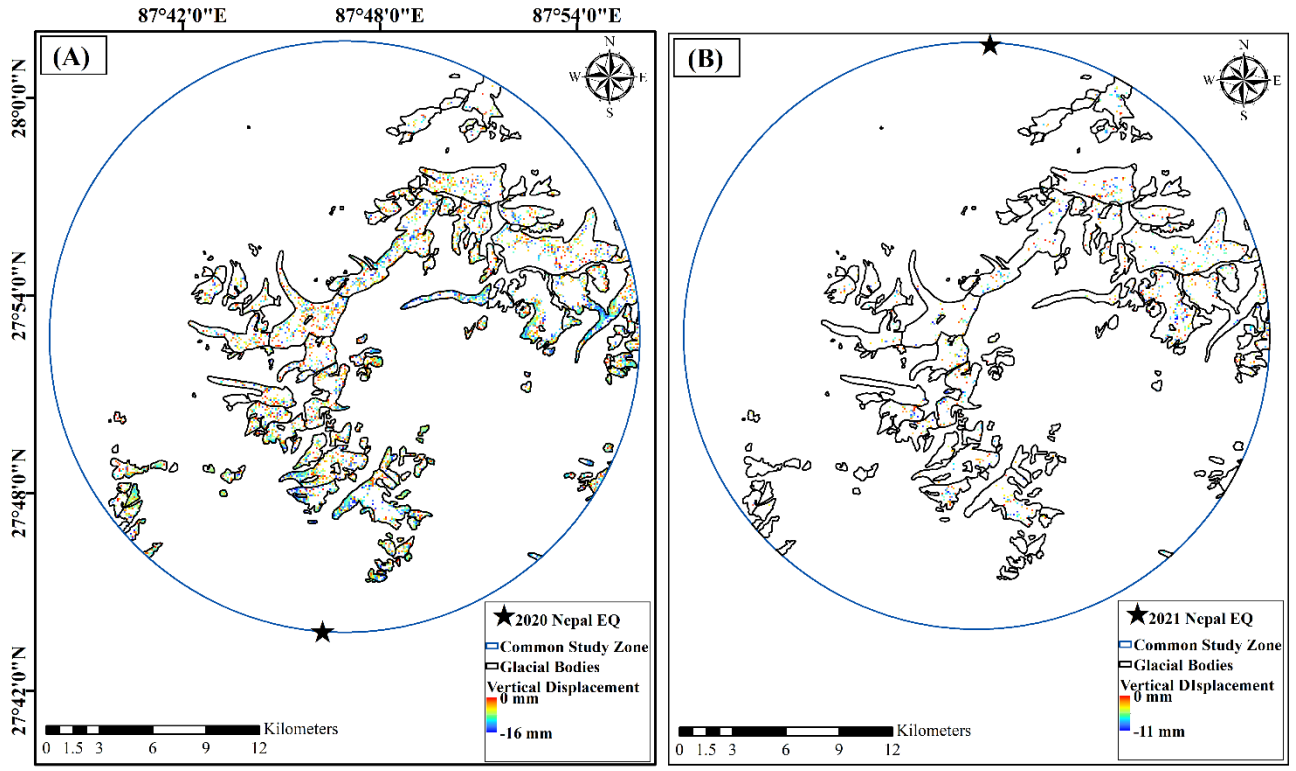


Figure 20. Map showing vertical displacement (mm) within glacial bodies of common study zone for (**A**) 2020 Nepal earthquake (M_W 4.1) and (**B**) 2021 Nepal earthquake (M_W 4.1).

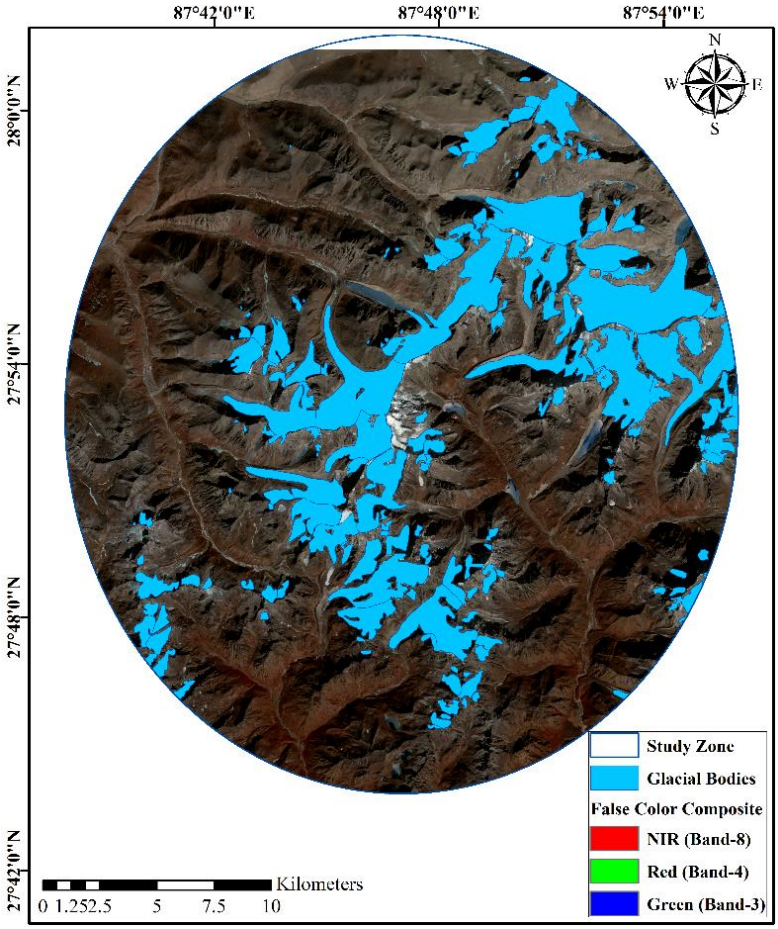


Figure 21. False-color-composite (FCC) map of the common study zone in Nepal.

5. Discussion

After investigating several earthquake events in the glaciated regions of Himalayan ranges, we see that DInSAR is an effective tool for investigating earthquake impacts in areas where other conventional techniques are tough to implement [79,80]. Where both magnitude and hypocentral depth play a paramount role in the detectability of an earthquake through C-band radar interferometry [70], this paper attempts to develop an understanding of seismic displacement of high-altitude Himalayan glaciated regions considering various categories of earthquakes. Shake maps can be used to determine the influence radius of earthquakes of higher magnitudes ($M_w \geq 4.5$), considering the minimum distance of the intensity-V MMI contour from the epicenter location, and normalized influence radii can be derived for lower-magnitude earthquakes for which shake maps are unavailable. Moreover, every earthquake is unique in terms of its impact on the Earth's surface. While some earthquake events, such as the 2020 Tibet earthquake [30], the 2017 Sikkim earthquake, and the 2021 and 2021 Nepal earthquakes, resulted in subsidence, other seismic events, such as the 2017 Thang earthquake, 2020 Leh earthquake, and 2021 Joshirmath earthquake, resulted in both uplift and subsidence.

As observed from multiple earthquake events, the seismic impact on solid earth regions and glacial bodies shows significant variation in terms of seismic displacements. The vertical displacement of a glacial mass is much higher than that of the solid earth for a particular earthquake, which suggests seismic amplification due to the presence of metamorphosed glacial ice over the ground surface. Moreover, the increased vertical displacement of a glacial patch farther from the epicenter than a glacial patch close to the epicenter, as in the case of the 2017 Thang earthquake, suggests that site-specific

seismic amplification properties of glacial bodies play a role in the associated displacement. However, it is to be noted that glacial bodies are superimposed on top of the solid earth. Therefore, the vertical displacements identified via DInSAR may not be solely due to the glacial material alone but also to the composite displacement of both the glacial body and the solid earth beneath. This cannot be segregated using satellite-based techniques.

It should be noted that DInSAR is highly effective for measuring vertical displacements due to earthquakes. Its sensitivity to horizontal movements is considerably limited by several factors inherent to the complex topography of glaciers and to observational geometry. DInSAR is primarily sensitive to displacements along the radar LOS, which typically results in the vertical component being more accurately captured than the horizontal one [81,82]. Moreover, in complex topographic regions like glacial terrains, the influence of the radar look angle and terrain-induced distortions (such as layover and foreshortening) can reduce the reliability of horizontal measurements. As DInSAR technology is most suited for observing vertical movements, a more robust approach for comprehensive three-dimensional glacier deformation would involve combining DInSAR with additional ascending or descending tracks, modeling, or other observation techniques, such as global navigation satellite systems (GNSSs). Addressing these limitations and combining datasets could provide a more accurate representation of the glacier response, capturing both horizontal and vertical displacement in the context of seismic activity.

6. Conclusions

DInSAR has recently emerged as a powerful tool for studying various natural hazards in the Himalayan region, especially in the case of earthquakes, where every earthquake event is unique in terms of its source, magnitude, and impact. Therefore, we studied seismic events of varying magnitudes and hypocenter depths triggered in the proximity of different glaciated terrains of the Himalayan region using Sentinel-1A/B C-band DInSAR. The findings of this study are as follows:

The 2020 Tibet earthquake (M_w 5.7) results in significant subsidence near the epicenter, with a mean glacial displacement of -38.9 mm, though glaciers are located far from the epicenter. In the case of the 2020 Leh earthquake (M_w 5.3), vertical displacement lies in the range of 31 mm and -33 mm, with a mean displacement of -2.4 mm. The glacial bodies lying close to the epicenter show positive displacement, or uplift, that shifts towards subsidence as we move away from the epicenter. Similarly to the 2020 Leh earthquake, the 2017 Thang earthquake (M_w 5.2) results in vertical surface displacement that varies from 51 mm to -39 mm, indicating both uplift and subsidence. The mean displacement of the Earth's surface and the glacial bodies are -2.8 mm and -3.4 mm, respectively. A comparison of glacial and solid earth patches, unwrapped separately, followed by vertical displacement, shows much greater values of seismic displacement for glacial patches that vary up to -173 mm and -576 mm. This exceeds the range of displacements for the solid earth surface by a large offset, considering either small patches or the entire influence area of the earthquake. Moreover, glacial patches farther from the epicenter but surrounded by larger glacial bodies show larger values of vertical displacement than glacial patches closer to the epicenter, indicating the presence of site-specific seismic amplification properties of glaciers. The 2021 Joshimath (M_w 4.5) earthquake displays reduced coherence near glaciers and vertical displacements of up to -94 mm in glacial patches. Conversely, smaller earthquakes like 2017 Sikkim (M_w 4.2) and 2018 Sikkim (M_w 4.4) show minimal displacement, with no impact from deeper hypocenters. And lastly the 2020 and 2021 Nepal earthquakes both with the same magnitude (M_w 4.1) at almost the same distance from the glacial bodies but having different hypocenter depths show that a shallower earthquake has more impact on glacial bodies in terms of vertical displacement than a deeper one.

Thus, earthquake events around Himalayan glaciers can be well studied with the help of C-band SAR interferometry, where other geodetic and photogrammetric techniques are hard to implement. Moreover, the continuous data acquisition of orbiting radars at a certain temporal offset makes them effective in studying earthquakes which are very unpredictable in terms of their triggering location and magnitude.

Glacial bodies are dense and thick envelopes of metamorphosed ice that may not reproduce similar deformation as the solid earth surface and may result in a site-specific amplification of seismicity. This suggests that because glaciers are different in composition and behavior, their response to seismic tremors is also different. As glaciers have viscoelastic properties, earthquakes, in terms of both associated deformation and response to seismic waves, may impact a glacial mass differently than solid bedrock. Future research into the dynamics behind the seismic deformation and amplification of glacial bodies should incorporate extensive modeling of that interaction.

As observed from analyzing multiple earthquake events, glacial mass studied separately using DInSAR reveals site-specific seismic amplification compared to the solid earth surface. However, glacial bodies are thick chunks of metamorphosed ice lying over the ground underneath. Therefore, the vertical displacement of glacial bodies registered using DInSAR is likely to show the results of the composite displacement of both the glacier and the solid earth surface at the glacier's base. Developing a better understanding of the impact of seismicity on glaciers will require additional studies, including the modeling of glacial properties and processes, into the material and dynamic properties of glacial bodies.

This study indicates that earthquake events can have a disproportionate impact on glaciers compared to the surrounding terrain due to the fragile and dynamic nature of glacial ice. Even relatively mild seismic activity can destabilize glacier masses, triggering hazards such as glacial surging, ice avalanches, landslides, and the catastrophic failure of moraine- or ice-dammed glacial lakes. The interaction between seismic waves and glaciers is influenced by glacial geomorphology, including slope, crevassing, and ice thickness, as well as geological and lithological factors that determine how seismic energy propagates through bedrock and sediments. In steep high-altitude environments, the amplification of ground motion can accelerate ice flow, induce fracturing, or destabilize moraine dams, leading to devastating downstream impacts. By integrating seismic hazard assessments with remote sensing, geophysical surveys, and numerical modeling, researchers can better identify glacial regions at risk and develop effective mitigation strategies. Understanding these interactions is crucial for early warning systems, infrastructure planning, and disaster risk reduction in seismically active glacierized regions.

Supplementary Materials: The following supporting information can be downloaded at: https://www.mdpi.com/article/10.3390/rs17050911/s1.

Author Contributions: S.K.M.: conceptualization, formal analysis, software, writing—original draft. R.B.: conceptualization, supervision, writing—review and editing. K.F.T.: conceptualization, writing—review and editing. All authors have read and agreed to the published version of the manuscript.

Funding: This research received no external funding.

Data Availability Statement: The datasets used in this study are available for download from the web portals mentioned as follows: Sentinel-1 SLC datasets: https://search.asf.alaska.edu/#/; Sentinel-2 MSI datasets: https://browser.dataspace.copernicus.eu/; ZTD Maps: http://www.gacos.net/; glacial shapefiles: https://www.glims.org/RGI/.

Acknowledgments: We are grateful to the European Space Agency (ESA), Alaska Satellite Facility (ASF), United States Geological Survey (USGS), and Randolph Glacier Inventory (RGI 6.0) supplemental to the Global Land Ice Measurements from Space initiative (GLIMS) for their tremendous efforts to make the data available for the current study.

Conflicts of Interest: The authors declare no potential competing interests that could have influenced the study reported in this paper.

References

1. Dyurgerov, M.B.; Meier, M.F. Mass balance of mountain and subpolar glaciers: A new global assessment for 1961–1990. *Arct. Alp. Res.* **1997**, *29*, 379–391. [CrossRef]
2. Zwally, H.J.; Abdalati, W.; Herring, T.; Larson, K.; Saba, J.; Steffen, K. Surface melt-induced acceleration of Greenland ice-sheet flow. *Science* **2002**, *297*, 218–222. [CrossRef] [PubMed]
3. Joughin, I.; Das, S.B.; King, M.A.; Smith, B.E.; Howat, I.M.; Moon, T. Seasonal speedup along the western flank of the Greenland Ice Sheet. *Science* **2008**, *320*, 781–783. [CrossRef]
4. Scherler, D.; Strecker, M.R. Large surface velocity fluctuations of Biafo Glacier, central Karakoram, at high spatial and temporal resolution from optical satellite images. *J. Glaciol.* **2012**, *58*, 569–580. [CrossRef]
5. Satyabala, S.P. Spatiotemporal variations in surface velocity of the Gangotri glacier, Garhwal Himalaya, India: Study using synthetic aperture radar data. *Remote Sens. Environ.* **2016**, *181*, 151–161. [CrossRef]
6. Berthier, E.; Vadon, H.; Baratoux, D.; Arnaud, Y.; Vincent, C.; Feigl, K.L.; Remy, F.; Legresy, B. Surface motion of mountain glaciers derived from satellite optical imagery. *Remote Sens. Environ.* **2005**, *95*, 14–28. [CrossRef]
7. Kumar, V.; Venkataramana, G.; Høgda, K.A. Glacier surface velocity estimation using SAR interferometry technique applying ascending and descending passes in Himalayas. *Int. J. Appl. Earth Obs. Geoinf.* **2011**, *13*, 545–551. [CrossRef]
8. Bhambri, R.; Bolch, T.; Chaujar, R.K. Frontal recession of Gangotri Glacier, Garhwal Himalayas, from 1965 to 2006, measured through high-resolution remote sensing data. *Curr. Sci.* **2012**, *102*, 489–494. [CrossRef]
9. Bhardwaj, A.; Joshi, P.K.; Sam, L.; Singh, M.K.; Singh, S.; Kumar, R. Applicability of Landsat 8 data for characterizing glacier facies and supraglacial debris. *Int. J. Appl. Earth Obs. Geoinf.* **2015**, *38*, 51–64. [CrossRef]
10. Thakur, P.K.; Dixit, A.; Chouksey, A.; Aggarwal, S.P.; Kumar, A.S. Ice sheet features identification, glacier velocity estimation, and glacier zones classification using high-resolution optical and SAR data. In *Land Surface and Cryosphere Remote Sensing III*; International Society for Optics and Photonics: Bellingham, DC, USA, 2016; Volume 9877, p. 987719. [CrossRef]
11. Thakur, P.K.; Aggarwal, S.P.; Arun, G.; Sood, S.; Senthil Kumar, A.; Mani, S.; Dobhal, D.P. Estimation of snow cover area, snow physical properties and glacier classification in parts of western Himalayas using C-band SAR data. *J. Indian Soc. Remote Sens.* **2017**, *45*, 525–539. [CrossRef]
12. Wagnon, P.; Linda, A.; Arnaud, Y.; Kumar, R.; Sharma, P.; Vincent, C.; Pottakkal, J.G.; Berthier, E.; Ramanathan, A.; Hasnain, S.I.; et al. Four years of mass balance on Chhota Shigri Glacier, Himachal Pradesh, India, a new benchmark glacier in the western Himalaya. *J. Glaciol.* **2007**, *53*, 603–611. [CrossRef]
13. Dobhal, D.P.; Gergan, J.T.; Thayyen, R.J. Mass balance studies of the Dokriani Glacier from 1992 to 2000, Garhwal Himalaya, India. *Bull. Glaciol. Res.* **2008**, *25*, 9–17.
14. Bhambri, R.; Bolch, T.; Chaujar, R.K.; Kulshreshtha, S.C. Glacier changes in the Garhwal Himalaya, India, from 1968 to 2006 based on remote sensing. *J. Glaciol.* **2011**, *57*, 543–556. [CrossRef]
15. Azam, M.F.; Wagnon, P.; Vincent, C.; Ramanathan, A.; Linda, A.; Singh, V.B. Reconstruction of the annual mass balance of Chhota Shigri glacier, Western Himalaya, India, since 1969. *Ann. Glaciol.* **2014**, *55*, 69–80. [CrossRef]
16. Pratap, B.; Dobhal, D.P.; Bhambri, R.; Mehta, M.; Tewari, V.C. Four decades of glacier mass balance observations in the Indian Himalaya. *Reg. Environ. Change* **2016**, *16*, 643–658. [CrossRef]
17. Li, Y.; Jiang, W.; Zhang, J.; Li, B.; Yan, R.; Wang, X. Sentinel-1 SAR-Based coseismic deformation monitoring service for rapid geodetic imaging of global earthquakes. *Nat. Hazards Res.* **2021**, *1*, 11–19. [CrossRef]
18. Goldstein, R.M.; Engelhardt, H.; Kamb, B.; Frolich, R.M. Satellite radar interferometry for monitoring ice sheet motion: Application to an Antarctic ice stream. *Science* **1993**, *262*, 1525–1530. [CrossRef]
19. Strozzi, T.; Luckman, A.; Murray, T.; Wegmuller, U.; Werner, C.L. Glacier motion estimation using SAR offset-tracking procedures. *IEEE Trans. Geosci. Remote Sens.* **2002**, *40*, 2384–2391. [CrossRef]
20. Leinss, S.; Wicki, R.; Holenstein, S.; Baffelli, S.; Bühler, Y. Snow avalanche detection and mapping in multitemporal and multiorbital radar images from TerraSAR-X and Sentinel-1. *Nat. Hazards Earth Syst. Sci.* **2020**, *20*, 1783–1803. [CrossRef]
21. Mondal, S.K.; Bharti, R. Detection Of Snow Avalanches Of 17th January 2020 Around Annapurna Mountain Range Using Multitemporal Radar Imageries of Sentinel-1. In Proceedings of the 2022 IEEE International Geoscience and Remote Sensing Symposium IGARSS, Kuala Lumpur, Malaysia, 17–22 July 2022. [CrossRef]
22. Mondal, S.K.; Bharti, R. Glacial burst triggered by triangular wedge collapse: A study from Trisul Mountain near Ronti glacier valley. *Geomat. Nat. Hazards Risk* **2022**, *13*, 830–853. [CrossRef]
23. Cochachin, A.; Frey, H.; Huggel, C.; Strozzi, T.; Büechi, E.; Cui, F.; Flores, A.; Saito, C. Integrated satellite InSAR and slope stability modeling to support hazard assessment at the Safuna Alta glacial lake, Peru. In *EGU General Assembly Conference Abstracts*. 2017; p. 14505. Available online: https://ui.adsabs.harvard.edu/abs/2017EGUGA..1914505C/abstract (accessed on 27 September 2018).

24. Scapozza, C.; Ambrosi, C.; Cannata, M.; Strozzi, T. Glacial lake outburst flood hazard assessment by satellite Earth observation in the Himalayas (Chomolhari area, Bhutan). *Geogr. Helv.* **2019**, *74*, 125–139. [CrossRef]
25. Mondal, S.K.; Narayan, J.; Sharma, C.; Bharti, R.; Dwivedy, S.K.; Chowdhury, P.R.; Singh, R.P. Glacial lakes outburst susceptibility and risk in the Eastern Himalayas using analytical hierarchy process and backpropagation neural network models. *Geomat. Nat. Hazards Risk* **2025**, *16*, 2449134. [CrossRef]
26. Riedel, B.; Walther, A. InSAR processing for the recognition of landslides. *Adv. Geosci.* **2008**, *14*, 189–194. [CrossRef]
27. Zhang, Y.; Meng, X.; Jordan, C.; Novellino, A.; Dijkstra, T.; Chen, G. Investigating slow-moving landslides in the Zhouqu region of China using InSAR time series. *Landslides* **2018**, *15*, 1299–1315. [CrossRef]
28. Mondal, S.K.; Narayan, J.; Bharti, R.; Dwivedy, S.K. Analytical Hierarchy and Neural Network based Landslide Risk Assessment at Sikkim, India: A Comparative Study. In Proceedings of the 2022 IEEE International Conference on Electronics, Computing and Communication Technologies (CONECCT), Bangalore, India, 8–10 July 2022; IEEE: Piscataway, NJ, USA, 2022. [CrossRef]
29. Thomas, A. Mapping of surface deformation associated with the 5.2 magnitude Stilfontein earthquake of 3 April 2017 using radar interferometry. *Egypt. J. Remote Sens. Space Sci.* **2021**, *24*, 85–108. [CrossRef]
30. Li, C.; Li, Q.; Tan, K.; Huang, Y.; Lu, X. Ground Deformation and Source Fault Model of the Mw 5.7 Xegar (Tibetan Plateau) 2020 Earthquake, Based on InSAR Observation. *Pure Appl. Geophys.* **2022**, *179*, 3589–3603. [CrossRef]
31. Mondal, S.K.; Bharti, R. Seismic Impact Around Himalayan Snow-Melt Fed Lake Using InSAR: A Case Study For 20 March 2020 MW5.7 Tibet Earthquake. In Proceedings of the 2022 IEEE International Geoscience and Remote Sensing Symposium IGARSS, Kuala Lumpur, Malaysia, 17–22 July 2022. [CrossRef]
32. Howell, S.E.; Komarov, A.S.; Dabboor, M.; Montpetit, B.; Brady, M.; Scharien, R.K.; Mahmud, M.S.; Nandan, V.; Geldsetzer, T.; Yackel, J.J. Comparing L-and C-band synthetic aperture radar estimates of sea ice motion over different ice regimes. *Remote Sens. Environ.* **2018**, *204*, 380–391. [CrossRef]
33. Jelenek, J.; Kopačková-Strnadová, V. Synergic use of Sentinel-1 and Sentinel-2 data for automatic detection of earthquake-triggered landscape changes: A case study of the 2016 Kaikoura earthquake (Mw 7.8), New Zealand. *Remote Sens. Environ.* **2021**, *265*, 112634. [CrossRef]
34. Gourmelen, N.; Kim, S.W.; Shepherd, A.; Park, J.W.; Sundal, A.V.; Björnsson, H.; Pálsson, F. Ice velocity determined using conventional and multiple-aperture InSAR. *Earth Planet. Sci. Lett.* **2011**, *307*, 156–160. [CrossRef]
35. Peltzer, G.; Rosen, P. Surface displacement of the 17 May 1993 Eureka Valley, California, earthquake observed by SAR interferometry. *Science* **1995**, *268*, 1333–1336. [CrossRef]
36. Massonnet, D.; Briole, P.; Arnaud, A. Deflation of Mount Etna monitored by spaceborne radar interferometry. *Nature* **1995**, *375*, 567–570. [CrossRef]
37. Mouginot, J.; Scheuchl, B.; Rignot, E. Mapping of ice motion in Antarctica using synthetic-aperture radar data. *Remote Sens.* **2012**, *4*, 2753–2767. [CrossRef]
38. Samsonov, S.; Dille, A.; Dewitte, O.; Kervyn, F.; d'Oreye, N. Satellite interferometry for mapping surface deformation time series in one, two and three dimensions: A new method illustrated on a slow-moving landslide. *Eng. Geol.* **2020**, *266*, 105471. [CrossRef]
39. Devaraj, S.; Yarrakula, K. Assessment of topographical and atmospheric errors in Sentinel 1 derived DInSAR. *Geocarto Int.* **2020**, *37*, 2424–2440. [CrossRef]
40. Crosetto, M.; Solari, L.; Mróz, M.; Balasis-Levinsen, J.; Casagli, N.; Frei, M.; Oyen, A.; Moldestad, D.A.; Bateson, L.; Guerrieri, L.; et al. The evolution of wide-area DInSAR: From regional and national services to the European Ground Motion Service. *Remote Sens.* **2020**, *12*, 2043. [CrossRef]
41. Kumar, V.; Venkataraman, G.; Rao, Y.S. SAR interferometry and speckle tracking approach for glacier velocity estimation using ERS-1/2 and TerraSAR-X spotlight high resolution data. In Proceedings of the 2009 IEEE International Geoscience and Remote Sensing Symposium, Cape Town, South Africa, 12–17 July 2009; Volume 5, p. V–332. [CrossRef]
42. Varugu, B.K.; Singh, M.; Rao, Y.S. Glacier velocity estimation using high resolution SAR images–Application to Gangotri glacier in Himalayas. In Proceedings of the (CD) of National Symposium on Geomatics for Digital India–Annual Conventions of Indian Society of Remote Sensing and Indian Society of Geomatics (ISRS-ISG), Jaipur, India, 13 June 2015.
43. Thakur, P.K.; Garg, V.; Nikam, B.R.; Singh, S.; Chouksey, A.D.P.R.; Dhote, P.R.; Aggarwal, S.P.; Chauhan, P.; Kumar, A.S. Snow cover and glacier dynamics study using c-and l-band SAR datasets in parts of North West Himalaya. *Int. Arch. Photogramm. Remote Sens. Spat. Inf. Sci.* **2018**, *42*, 375–382. [CrossRef]
44. Lal, P.; Vaka, D.S.; Rao, Y.S. Mapping surface flow velocities of Siachen and Gangotri glaciers using TerraSAR-X and Sentinel-1A data by intensity tracking. *ISPRS Ann. Photogramm. Remote Sens. Spat. Inf. Sci.* **2018**, *4*, 325–329. [CrossRef]
45. Yang, Y.; Chen, Q.; Xu, Q.; Liu, G.; Hu, J.C. Source model and Coulomb stress change of the 2015 Mw 7.8 Gorkha earthquake determined from improved inversion of geodetic surface deformation observations. *J. Geod.* **2019**, *93*, 333–351. [CrossRef]
46. Wang, T.; Wei, S.; Shi, X.; Qiu, Q.; Li, L.; Peng, D.; Weldon, R.J.; Barbot, S. The 2016 Kaikōura earthquake: Simultaneous rupture of the subduction interface and overlying faults. *Earth Planet. Sci. Lett.* **2018**, *482*, 44–51. [CrossRef]

47. Yasuda, T.; Furuya, M. Short-term glacier velocity changes at West Kunlun Shan, Northwest Tibet, detected by synthetic aperture radar data. *Remote Sens. Environ.* **2013**, *128*, 87–106. [CrossRef]
48. Milillo, P.; Rignot, E.; Mouginot, J.; Scheuchl, B.; Morlighem, M.; Li, X.; Salzer, J.T. On the short-term grounding zone dynamics of Pine Island Glacier, West Antarctica, observed with COSMO-SkyMed interferometric data. *Geophys. Res. Lett.* **2017**, *44*, 10–436. [CrossRef]
49. Rajendran, K.; Parameswaran, R.M.; Rajendran, C.P. Seismotectonic perspectives on the Himalayan arc and contiguous areas: Inferences from past and recent earthquakes. *Earth-Sci. Rev.* **2017**, *173*, 1–30. [CrossRef]
50. Thakur, V.C. Active tectonics of Himalayan frontal fault system. *Int. J. Earth Sci.* **2013**, *102*, 1791–1810. [CrossRef]
51. Hubbard, M.S.; Harrison, T.M. 40Ar/39Ar age constraints on deformation and metamorphism in the Main Central Thrust zone and Tibetan Slab, eastern Nepal Himalaya. *Tectonics* **1989**, *8*, 865–880. [CrossRef]
52. Meigs, A.J.; Burbank, D.W.; Beck, R.A. Middle-late Miocene (> 10 Ma) formation of the Main Boundary thrust in the western Himalaya. *Geology* **1995**, *23*, 423–426. [CrossRef]
53. Thakur, V.C.; Pandey, A.K.; Suresh, N. Late Quaternary–Holocene evolution of dun structure and the Himalayan Frontal fault zone of the Garhwal sub-Himalaya, NW India. *J. Asian Earth Sci.* **2007**, *29*, 305–319. [CrossRef]
54. Mondal, S.K.; Bharti, R.; Tiampo, K. Seismic Deformations due to 2023 Nepal Earthquake Sequence using Satellite Remote Sensing Techniques. In *EGU General Assembly Conference Abstracts*. 2024, p. 17792. Available online: http://doi.org/10.5194/egusphere-egu24-17792 (accessed on 27 September 2018).
55. Winsvold, S.H.; Kääb, A.; Nuth, C.; Andreassen, L.M.; Van Pelt, W.J.; Schellenberger, T. Using SAR satellite data time series for regional glacier mapping. *Cryosphere* **2018**, *12*, 867–890. [CrossRef]
56. ESA. *Interferometric Wide Swath, User Guides, Sentinel-1 SAR*; ESA: Paris, France, 2016. Available online: https://sentinel.esa.int/web/sentinel/user-guides/sentinel-1-sar/acquisition%20modes/interferometric-wide-swath (accessed on 27 September 2018).
57. RGI Consortium. *Randolph Glacier Inventory—A Dataset of Global Glacier Outlines: Version 6.0: Technical Report, Global Land Ice Measurements From Space*; Digital Media; RGI Consortium: Boulder, CO, USA, 2017. [CrossRef]
58. Moreira, A.; Prats-Iraola, P.; Younis, M.; Krieger, G.; Hajnsek, I.; Papathanassiou, K.P. A tutorial on synthetic aperture radar. *IEEE Geosci. Remote Sens. Mag.* **2013**, *1*, 6–43. [CrossRef]
59. Rabus, B.; Eineder, M.; Roth, A.; Bamler, R. The shuttle radar topography mission—A new class of digital elevation models acquired by spaceborne radar. *ISPRS J. Photogramm. Remote Sens.* **2003**, *57*, 241–262. [CrossRef]
60. Yagüe-Martínez, N.; Prats-Iraola, P.; Gonzalez, F.R.; Brcic, R.; Shau, R.; Geudtner, D.; Eineder, M.; Bamler, R. Interferometric processing of Sentinel-1 TOPS data. *IEEE Trans. Geosci. Remote Sens.* **2016**, *54*, 2220–2234. [CrossRef]
61. Zhou, X.; Chang, N.B.; Li, S. Applications of SAR interferometry in earth and environmental science research. *Sensors* **2009**, *9*, 1876–1912. [CrossRef] [PubMed]
62. Goldstein, R.M.; Werner, C.L. Radar interferogram filtering for geophysical applications. *Geophys. Res. Lett.* **1998**, *25*, 4035–4038. [CrossRef]
63. Chen, C.W.; Zebker, H.A. Phase unwrapping for large SAR interferograms: Statistical segmentation and generalized network models. *IEEE Trans. Geosci. Remote Sens.* **2002**, *40*, 1709–1719. [CrossRef]
64. Hellwich, O.; Ebner, H. Geocoding SAR interferograms by least squares adjustment. *ISPRS J. Photogramm. Remote Sens.* **2000**, *55*, 277–288. [CrossRef]
65. Walter, D. Surface Subsidence Monitoring with NEST. Tutorial—SAR Interferometry. Institute of Geotechnical Engineering and Mine Surveying, TU Clausthal. 2014. Available online: https://eo-college.org/resource/insar_deformation/ (accessed on 27 September 2018).
66. Yu, C.; Penna, N.T.; Li, Z. Generation of real-time mode high-resolution water vapor fields from GPS observations. *J. Geophys. Res. Atmos.* **2017**, *122*, 2008–2025. [CrossRef]
67. Yu, C.; Li, Z.; Penna, N.T. Interferometric synthetic aperture radar atmospheric correction using a GPS-based iterative tropospheric decomposition model. *Remote Sens. Environ.* **2018**, *204*, 109–121. [CrossRef]
68. Yu, C.; Li, Z.; Penna, N.T.; Crippa, P. Generic atmospheric correction model for interferometric synthetic aperture radar observations. *J. Geophys. Res. Solid Earth* **2018**, *123*, 9202–9222. [CrossRef]
69. Li, X.; Huang, G.; Kong, Q. Atmospheric phase delay correction of D-InSAR based on Sentinel-1A. *Int. Arch. Photogramm. Remote Sens. Spat. Inf. Sci.* **2018**, 955–960. [CrossRef]
70. Mellors, R.J.; Magistrale, H.; Earle, P.; Cogbill, A. Comparison of four moderate-size earthquakes in southern California using seismology and InSAR. *Bull. Seismol. Soc. Am.* **2004**, *94*, 2004–2014. [CrossRef]
71. Rosen, P.A.; Gurrola, E.; Sacco, G.F.; Zebker, H. The InSAR scientific computing environment. In Proceedings of the EUSAR 2012 9th European Conference on Synthetic Aperture Radar, Nuremberg, Germany, 23–26 April 2012; pp. 730–733.
72. Fielding, E.J.; Jung, J. Damage Proxy Mapping with SAR interferometric coherence change. *Procedia Comput. Sci.* **2024**, *239*, 2322–2328. [CrossRef]

73. Zebker, H.A.; Villasenor, J. Decorrelation in interferometric radar echoes. *IEEE Trans. Geosci. Remote Sens.* **1992**, *30*, 950–959. [CrossRef]
74. Krishan, A. The habitat of two deserts in India: Hot-dry desert of Jaisalmer (Rajasthan) and the cold-dry high altitude mountainous desert of Leh (Ladakh). *Energy Build.* **1996**, *23*, 217–229. [CrossRef]
75. Reeh, N.; Christensen, E.L.; Mayer, C.; Olesen, O.B. Tidal bending of glaciers: A linear viscoelastic approach. *Ann. Glaciol.* **2003**, *37*, 83–89. [CrossRef]
76. *BIS-1893*; Criteria for Earthquake Resistant Design of Structures-Part-1, General Provisions and Buildings. Bureau of Indian Standards: New Delhi, India, 2002.
77. Lohman, R.B.; Simons, M. Locations of selected small earthquakes in the Zagros mountains. *Geochem. Geophys. Geosystems* **2005**, *6*. [CrossRef]
78. Funning, G.J.; Garcia, A. A systematic study of earthquake detectability using Sentinel-1 Interferometric Wide-Swath data. *Geophys. J. Int.* **2019**, *216*, 332–349. [CrossRef]
79. Papadopoulos, G.A.; Agalos, A.; Karavias, A.; Triantafyllou, I.; Parcharidis, I.; Lekkas, E. Seismic and geodetic imaging (DInSAR) investigation of the March 2021 strong earthquake sequence in Thessaly, central Greece. *Geosciences* **2021**, *11*, 311. [CrossRef]
80. Dalal, P.; Senapati, B.; Kundu, B. Co-seismic surface displacement of the June 21, 2022 M_W6 Khōst, Afghanistan earthquake from InSAR observations. *Geod. Geodyn.* **2024**, *15*, 201–208. [CrossRef]
81. Hu, J.; Li, Z.W.; Ding, X.L.; Zhu, J.J.; Zhang, L.; Sun, Q. Resolving three-dimensional surface displacements from InSAR measurements: A review. *Earth-Sci. Rev.* **2014**, *133*, 1–17. [CrossRef]
82. Dai, K.; Deng, J.; Xu, Q.; Li, Z.; Shi, X.; Hancock, C.; Wen, N.; Zhang, L.; Zhuo, G. Interpretation and sensitivity analysis of the InSAR line of sight displacements in landslide measurements. *GIScience Remote Sens.* **2022**, *59*, 1226–1242. [CrossRef]

Disclaimer/Publisher's Note: The statements, opinions and data contained in all publications are solely those of the individual author(s) and contributor(s) and not of MDPI and/or the editor(s). MDPI and/or the editor(s) disclaim responsibility for any injury to people or property resulting from any ideas, methods, instructions or products referred to in the content.